Competitive adsorption of ZrO2 nanoparticle and alkali cations (Li+ – Cs+) on muscovite (001)

Qiu, C.; Eng, P. J.; Hennig, C.; Schmidt, M.;

Originally published:

October 2018

Langmuir 34(2018)41, 12270-12278

DOI: https://doi.org/10.1021/acs.langmuir.8b02277

Competitive adsorption of ZrO_2 nanoparticle and alkali cations (Li^+ – Cs^+) on muscovite (001)

Canrong Qiu,[1] Peter J. Eng,[2] Christoph Hennig,[1] Moritz Schmidt[1,*]

[1] Helmholtz-Zentrum Dresden-Rossendorf, Institute of Resource Ecology, Dresden, Germany

[2] Center for Advanced Radiation Sources, University of Chicago, Chicago, IL 60637, USA

[*]Corresponding author: Tel.: +49 351 260 3136; E-mail address: moritz.schmidt@hzdr.de

Abstract

We studied the adsorption behavior of ZrO_2 nanoparticles on muscovite (001) surface in the presence of cations from the alkali series (Li^+, Na^+, K^+, Rb^+ and Cs^+). The results of X-ray reflectivity, i.e. specular crystal truncation rod and resonant anomalous X-ray reflectivity in combination with AFM images, show that the sorption of ZrO_2 nanoparticles is significantly affected by the binding mode of alkali ions on the muscovite (001) surface. From solutions containing alkali ions binding as outer sphere surface complexes (i.e. Li^+ and Na^+), higher uptake of Zr^{4+} is observed corresponding to the binding of larger nanoparticles, which relatively easily replaces the loosely bound alkali ions. However, Zr^{4+} uptake in solutions containing alkali ions binding as inner sphere surface complexes (i.e. K^+, Rb^+, and Cs^+) is significantly lower and smaller nanoparticles are found at the interface. In addition, uptake of Zr^{4+} in the presence of inner sphere bound cations displays a strong linear relationship with hydration energy of the coexisting alkali ion. The linear trend can be interpreted as competitive adsorption between ZrO_2 nanoparticles and inner sphere bound alkali cations, which are replaced on the surface and undergo rehydration after release to the solution. The rehydration of alkali ion gives rise to a large energy gain, which dominates the reaction energy of the competitive adsorption process. The competitive adsorption mechanism of ZrO_2 nanoparticle and alkali ions is discussed comprehensively to highlight the potential relationship between the hydration effect of alkali ions and the effect of charge density of the nanoparticles.

Keywords: competitive sorption; background electrolytes; CTR; RAXR; surface X-ray diffraction; AFM; nanoparticles.

Introduction

The astonishing physical chemical and electronic properties of nanoparticles have triggered a great amount of interest in research fields relating to their industrial applications, such as advanced material science,[1, 2] green energy conversion,[3, 4] and novel drug design.[5, 6] Nanoparticles also play a critical role in different environmental settings through a variety of processes, such as contaminant retention and transport,[7] and bioavailability of elements.[8] In addition, technical applications of nanomaterials have led to an increased interest in nanoparticle toxicity and their fate in the environment.[9, 10] Nanoparticulate transport in the environment also

plays an important role for the mobility of highly radiotoxic actinides in the environment, for instance in the vicinity of highly contaminated "legacy sites".[11, 12] Yet, studies aiming to understand the sorption of nanoparticles on the molecular level remain relatively scarce[13, 14] and there are few studies that systematically focus on understand the reaction's dependency on basic aqueous chemistry. A recent study[15] revealed a highly unusual dependence of the adsorption of Th^{4+} on the muscovite (001) basal plane on the composition of the background electrolyte. Both, Li^+ and K^+ were found to enhance Th^{4+} uptake relative to Na^+, while ClO_4^- was found to have a detrimental effect compared to Cl^-. Only in the presence of Li^+ the formation of Th-(hydr)oxo-nanoparticles was observed. A partial explanation for this behavior may be found in the sorption behavior of the background electrolyte cations. For instance, the size difference of the alkali ions leads to changes in their strength of hydration, which decreases for larger ions.[16] As a result, these alkali ions behave differently when they are approaching a charged mineral surface. As shown by Lee et al.,[17] the weakly hydrated alkali ions (e.g. Rb^+, and Cs^+) tend to form inner sphere (IS) complexes at muscovite (001), where parts of the hydration shell are replaced by surface functional groups. More strongly hydrated cations (e.g. Li^+, and Na^+) instead form outer sphere (OS) with their hydration shell intact. In between, K^+ is present in both forms, IS and OS, with IS complexation dominating its speciation. Although the difference of adsorption chemistry of alkali ions on muscovite (001) surface has been comprehensively studied, it remains unclear how the alkali ions will impact the nanoparticle adsorption on a charged surface.

In this study, we chose ZrO_2 as a model nanoparticle to study its sorption behavior on the muscovite (001) surface in solutions containing different alkali ions. We have recently studied the aggregation mechanism of such nanoparticles in solutions of a fixed pH 2.5 and increasing ionic strength,[18] which points to a step-wise formation of nanoparticles containing a platelet-like morphology (i.e. larger lateral than vertical dimension). The surface net positive charge, accumulating at the nanoparticle edges, drives adsorption of nanoparticles on the mica surface through electrostatic attraction. We use these experiments as a baseline for studying the effect of background electrolyte composition on the adsorption of ZrO_2 nanoparticles. Surface sensitive techniques, including traditional AFM imaging as well as specular crystal truncation rod (CTR) diffraction and resonant anomalous X-ray reflectivity (RAXR), are used to characterize the size and distribution of nanoparticles deposited on muscovite (001) in the presence of 0.1 M solutions of ACl with A = Li^+ – Cs^+. In the case of Rb^+ we can use the same technique to visualize the distribution of the alkali ion within the interface in the presence of Zr nanoparticles. These results can then help to understand the mobility of metal oxide nanoparticles in the environment and potentially shed light on the unusual behavior observed for Th^{4+} under similar conditions.

Materials and experiments

Muscovite substrate

Muscovite ($KAl_2(AlSi_3O_{10})(OH, F)_2$) is a phyllosilicate that has a tetrahedral-octahedral-tetrahedral (TOT) layer structure, commonly seen in many other clay minerals. In muscovite, the isomorphous substitution of Si^{4+} with Al^{3+} gives rise to an excess $1e^-$ charge per area of the unit

cell, A_{UC} = 46.72 Å^2, equivalent to 0.021 e^-/Å^2. The structural negative charge is compensated by K^+ ions, which is located between TOT layers. A freshly cleaved muscovite exposes the K^+ ions, which dissociate when the surface is immersed in aqueous solution. The release of structural K^+ ions will produce a negatively charged muscovite surface,[19-21] which typically unselectively attracts cations and particles carrying positive surface charges through electrostatic bonding.

X-ray reflectivity measurement

Zr^{4+} solutions of 0.1 mM were prepared using $ZrOCl_2 \cdot 8H_2O$ (Sigma Aldrich, purity ≥ 99.5%). Five samples were prepared containing 0.1 M ACl (A=Li^+, Na^+, K^+, Rb^+, and Cs^+), corresponding to a total ionic strength of 102 mM when assuming no polymerization. The pH of Zr^{4+} solutions was adjusted to 2.5(±0.1) using NaOH and HCl. Each mica crystal of size 1.25×1.25 cm^2 and thickness 0.25 mm (Asheville Schoonmaker Mica Company) was cleaved prior to incubation in Zr^{4+} solutions for ~24 hours.

After incubation, a liquid sample cell (see Fig. S2), similar to the one used in our earlier work,[14]was used to ensure that the following X-ray measurement is performed under situ conditions. To mount crystals in the liquid cell, the mica sample was quickly removed from the incubation vial, transferred to the sample cell, and covered with an additional 100 µL Zr^{4+} solution. A liquid film of a thickness ~5 – 10 µm was trapped on the crystal surface using a thin Kapton membrane. This water layer is sufficiently thin to allow for transmission of X-rays, but thick enough to be representative of bulk water (i.e. > 30 Å for this system, see Fig. 3). Surface scattering measurements were performed in duplicate at the GSECARS undulator beamline 13-IDC at the Advanced Photon Source (APS), Argonne National Laboratory and the Rossendorf beamline BM-20 (ROBL) at the European Synchrotron Facility (ESRF). At GSECARS, the incoming X-ray (beam size = 100 µm×1000 µm) was directed on the surface of the sample mounted at a Kappa geometry Newport six-circle diffractometer (4S+2D). ROBL is equipped with an Eulerian-geometry 6-circle diffractometer (4S+2D) and has an incident beam size of 250 x 150 µm^2. At both beamlines, the energy of the incoming beam was adjusted using a liquid nitrogen cooled double-crystal silicon (1 1 1) monochromator, and the scattered X-ray intensity was measured using a Dectris Pilatus 100K 2D pixel array detector.[22] The X-ray reflectivity measurements were performed in both vertical (GSECARS) and horizontal (ROBL) mode to account for any gravitational accumulation of nanoparticles. No gravitational effects were observed, and results from both beamlines are in excellent agreement.

For X-ray reflectivity measurements, the energy of the incoming X-ray was fixed at 16,000 eV, which is well away from the Zr K edge (17,998 eV) to minimize resonant effects. We selected 21 unique values of momentum transfer *q*. RAXR measurements were performed at each value by scanning the energy of the incoming X-ray through the Zr K-edge. In addition, we also performed Rb RAXR measurements for the sample containing RbCl at the same q values by scanning the X-ray energy through the Rb K-edge (15,200 eV). The energy of Zr/Rb K-edge were determined on one sample (0.1 M RbCl, 0.1 mM Zr) through fluorescence XANES measurements collected in grazing-

incidence mode using an SII Vortex ME4 X-ray fluorescence detector. The normalized XANES spectrum was used to obtain the anomalous dispersion terms required for RAXR data analysis by applying the Kramers-Kronig transformation.[23]

AFM imaging

For each sample condition mentioned above, we also carried out AFM imaging in parallel. Prior to AFM measurements, each sample was prepared in the same way as for X-ray measurements. In situ AFM imaging was performed at room temperature (~25 ºC) in tapping mode using an Asylum Research Cypher AFM instrument equipped with a BRUKER MSNL-10 silicon tips on nitride cantilevers, between 26 and 50 kHz frequency, and force constant of 0.1 N/m. The AFM images were analyzed using the open source software Gwyddion.[24] In addition, we performed statistical analysis on each AFM image to obtain the height distribution as well as the lateral size of bound nanoparticles. The height distribution on each AFM image is obtained through normalizing each height value so that the maximum height percentage equals 100%, as shown in Fig. 4. The lateral size of nanoparticles was determined from one-dimensional texture profiles, after removing the contribution of roughness through an analysis of the high-frequency components of the profiles. The particles' lateral size can then be determined from the thus obtained low frequency contribution. (Fig. S9).

The size of the particles analyzed in this study is sufficiently small for tip artefacts to have a significant impact on measured particle sizes. Although tip artefacts are unavoidable in AFM measurements, all samples were measured with the same type of AFM tip so that any tip artefacts are comparable throughout our sample series. As such, the numerical values given below may differ from the particles' "real" dimensions, but any observed trends should nonetheless be significant.

CTR/RAXR model refinement

Both CTR and RAXR have been described in detail elsewhere.[25-27] Briefly, the specular (00L) crystal truncation rod,[26] oriented perpendicular to the surface, is a column of scattering intensity connecting Bragg peaks in reciprocal space. Refinement of a structure model to the CTR data will generate the total interfacial electron density that is a function of surface relaxation, adsorbed ions, and interfacial water. RAXR[28] is an element specific technique that probes the distribution of a resonant element registered at the scattering interface. Using a least-squares fitting routine, we performed model refinement to fit against experimental data with the corresponding CTR and RAXR data calculated from a parameterized structural model, which consists of the ideal muscovite substrate lattice, the interfacial region, and bulk water. The variation of interfacial structure attributes to the structural relaxation of atoms in the two top unit-cell layers of the muscovite surface and the presence of near-surface species such as adsorbed species and water. The distribution of each adsorbed species is described using a Gaussian peak, and the total structure factor *F* is expressed as

$$F = \sum_j c_j f_j(q) \exp(iqz_j) \exp\left[-\frac{q^2 u_j^2}{2}\right] \qquad (1),$$

where $f_j(q)$ is the atomic scattering factor and c_j, z_j, and u_j are the occupancy, height from the surface, and r.m.s. width of the j^{th} atom, respectively. Bulk water was expressed by a layered water-model.[29, 30] For RAXR the same fitting strategy is applied, and the Zr (or Rb) distribution was described as individual Gaussian peaks. The resonant structure factor is expressed as

$$F_R(q) = (f'(E) + if''(E)) \sum_j c_j \exp(iqz_j) \exp\left[-\frac{q^2 u_j^2}{2}\right] \quad (2),$$

where f'(E) and f''(E) are the anomalous dispersion terms of the resonant element, here Zr and Rb. The quality-of-fit of each CTR or RAXR model was characterized by a scaled χ^2 and an R-factor (see SI for details).

Results and discussions

Crystal truncation rods and resonant anomalous X-ray reflectivity

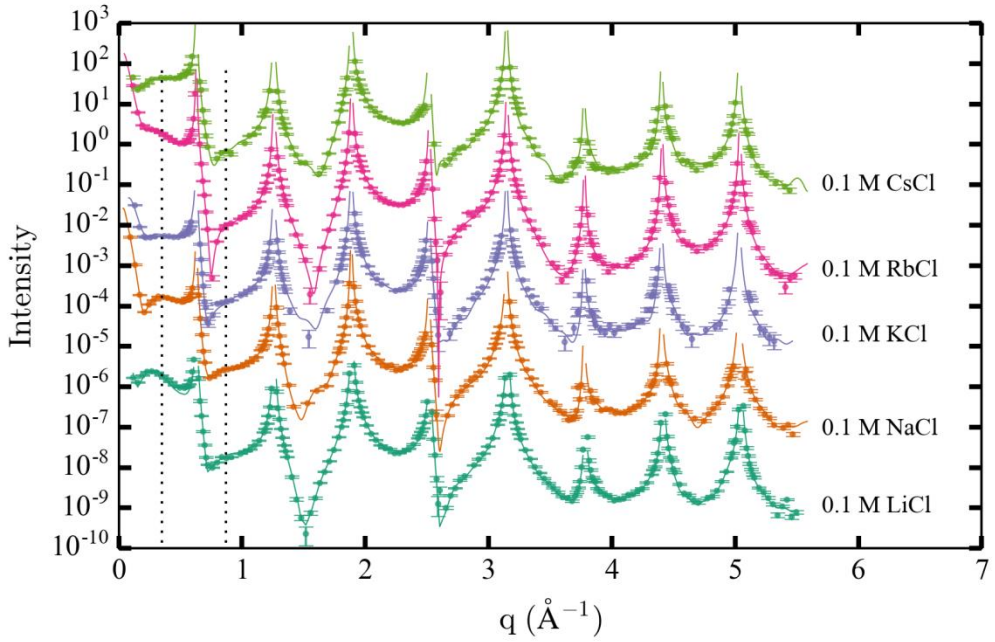

Figure 1. Specular CTR data measured from Zr(IV)/mica(001) samples (0.1 mM Zr solution of pH 2.5 reacting with freshly cleaved mica (001) for ~ 24 h) with 0.1 M LiCl (dark green), 0.1 M NaCl (orange), 0.1 M KCl (blue), 0.1 M RbCl (pink), and 0.1 M CsCl (light green). The associated specular CTR calculated based on the associated best fit models are illustrated as solid lines with the same color as the associated data points. Vertical offset (1 log unit stepwise) was applied to CTRs for ACl-containing Zr solutions for better comparison. Two vertical dashed lines highlight the CTR variation at low q values (q = 0.4 and 0.9 Å^{-1}) discussed in the text.

The best fit CTR/RAXR model results are compiled in Table S1. The surface substrate atoms display near-negligible relaxations, which dissipate quickly with increasing distance from the surface leaving lower atomic layers essentially unaffected.[31] Most models could reproduce the data reasonably well with $\chi^2 < 9$. We should also point out that the CTR fit for two samples (in

presence of KCl and CsCl) is relatively poor with large χ^2 values (20.8 and 19.1, respectively). The relatively poor fits are due to the rather simple structures used to fit the data. More complicated structure models containing more Gaussian peaks could lead to a better figures-of-merit, but led to covariance among the additional parameters. It is thus likely that some details in the two mentioned structures are not fully resolved in our models, the overall electron density distribution is however sound, especially as the Zr RAXR does not suffer from the same issues in either case. Fig. 1 shows CTR data as well as CTR modeling results of ZrNP adsorption on mica surface in the presence of different alkali ions. CTR intensities at low *q* values are significantly affected by the type of coexisting alkali ions. A broad peak at low *q* can be clearly recognized in Zr solution containing Li^+. This low *q* feature becomes less pronounced in solutions containing Na^+, and then disappears in K^+ solution, where the first midzone is essentially flat. After that, the low *q* region exhibits a once again different shape in Rb^+ solution. Interestingly, in the Cs^+ solution the first midzone shows an appearance intermediate between those found for Na^+ and K^+ solutions.

The momentum transfer *q* is an energy and substrate independent expression for the scattering angle 2θ: $q = 4\pi \sin(2\theta/2)/\lambda = 2\pi L/c_{proj,}$ where λ is the X-ray wavelength, *L* is the Miller index, c_{proj} is the value of lattice parameter c after being projected to surface normal direction. As *q* is a reciprocal space unit, changes at small values of *q* as described above relate to changes in large structures in real space, and vice versa. In the studied system, the adsorbed ZrO_2 nanoparticles represent the largest structural units at the mica-fluid interface, the broad vertical distribution of coexisting cation will also contribute to the total electron density up to 2 nm above mica surface, as seen in the Rb^+ structure (Fig.3). However, this broad distribution of Rb^+ is also related to the presence of the ZrO_2 nanoparticles as is evident from comparison with Rb^+ sorption structures in their absence.[17, 32] Consequently, the evolution of low *q* features observed in CTR profiles must be related to the fact that the ZrO_2 nanoparticle sorption behavior at mica surface has been modified by the coexisting alkali ions.

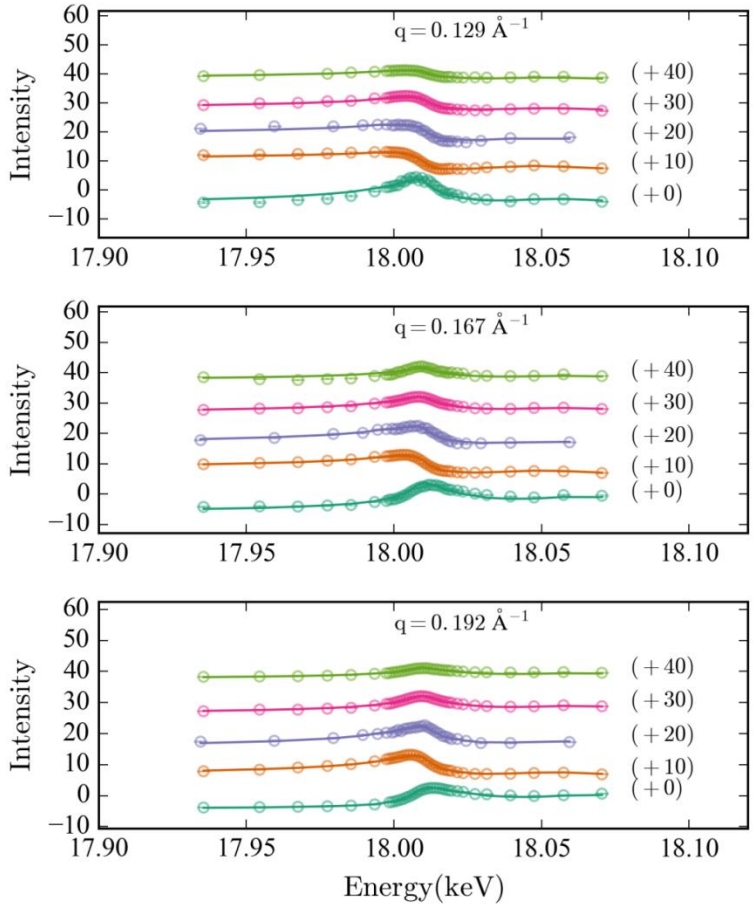

Figure 2. Representative RAXR data (open dots) as a function of the alkali ion type for Zr(IV) adsorption on the mica (001) surface as well as the calculated RAXR profiles from the best fit Zr model (solid lines). In each subplot, the data points and calculated lines display the results for Zr/mica interface in 0.1 M LiCl (dark green), NaCl (orange), KCl (blue), RbCl (pink) and CsCl (light green) from bottom to top, respectively. Each spectrum presents the variation of specular reflectivity as a function of photon energy, E, at fixed momentum transfer *q*. The specular reflectivity (data point and calculated values) at each *q* for different cases are offset for better visibility. See SI for the complete set of RAXR results.

RAXR results are illustrated in Fig 2, where RAXR scans for all samples are shown at three representative values of *q*, i.e. *q* = 0.129 $Å^{-1}$, 0.167 $Å^{-1}$ and 0.192 $Å^{-1}$. The most pronounced difference is observed in Li^+ solution, which gives rise to RAXR scans distinct from the other samples. The shape difference indicates a different average adsorption height of ZrO_2 nanoparticles under these conditions. The RAXR shape of the other alkali solutions (Na^+, K^+, Rb^+, Cs^+) are similar to each other but the modulation amplitude is decreasing continuously from Na^+ to Cs^+ suggesting decreasing uptake of Zr^{4+}.

Rb RAXR results are shown in Fig. S8, where we observed that the Rb-RAXR modulation appears throughout the whole *q* range, as opposed to Zr case with Zr-RAXR modulation damping quickly at q > 0.538 $Å^{-1}$. These RAXR modulations observed for Rb suggest that the interfacial structure must contain a sharp feature with a well-defined position relative to the mica surface.

Interfacial structure

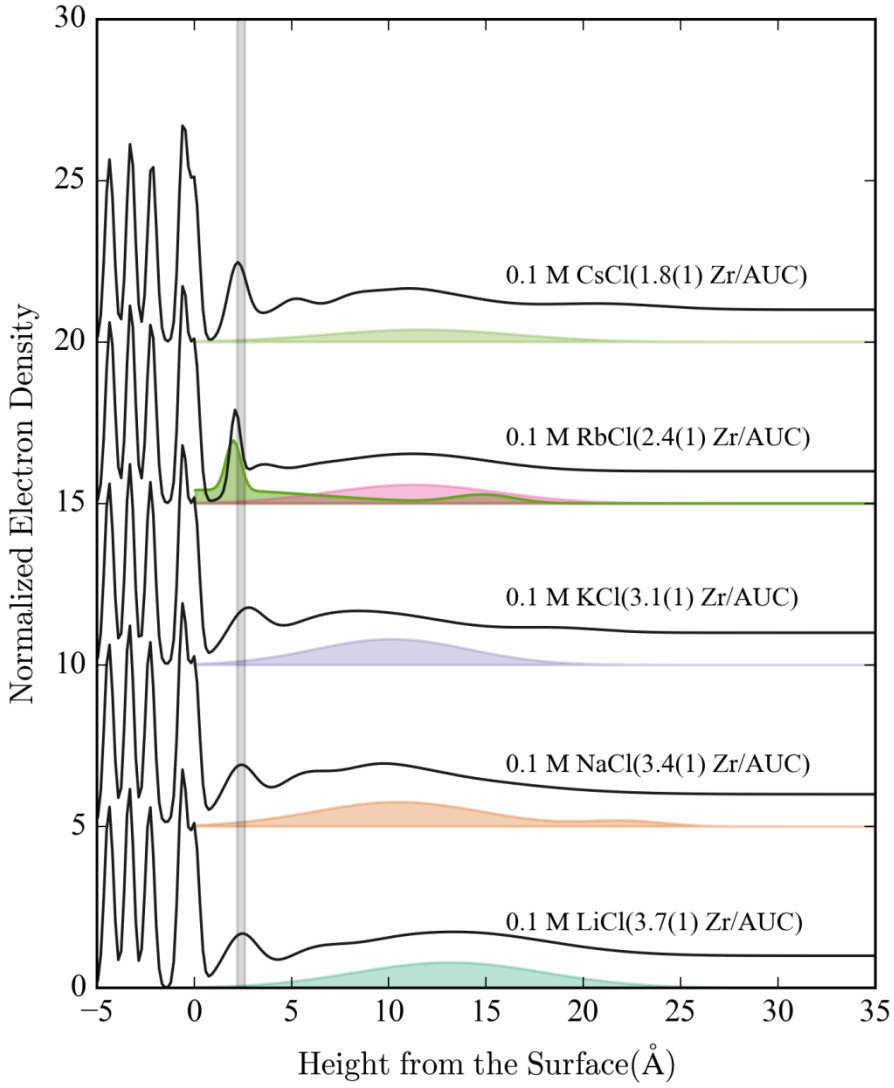

Figure 3. CTR-derived total electron density distributions (solid lines) and model-dependent RAXR-derived interfacial Zr and Rb electron density (filled peaks) above the mica (001) surface. The interfacial Rb structure for RbCl-Zr-mica sample is shown as green filled area partially overlapping with the Zr structure shown as pink filled area. The electron density values are normalized to that of bulk water ρ_{water} = 0.33 e^{-}/Å^3, values for (NaCl, KCl, RbCl and CsCl)-containing samples are shifted vertically for better visibility. Light black line highlights the common pronounced peaks at 2.5 Å in z direction.

The modeling of CTR and RAXR data produces the total election density profiles as well as the electron density distribution of a resonant element (here Zr), respectively, as illustrated in Fig. 3. The total electron density profiles are to some extent similar, with a relatively sharp feature at around 2.5 Å followed by a broader feature consisting of several partially overlapped Gaussian peaks (number of peaks ≤ 3). The first near-surface structure feature maintains its position at around 2.5 Å in all samples. The width of this peak barely changes from Li^+ to Na^+ solution, and

becomes slighter larger in K^+ solution, as opposed to Rb^+ and Cs^+ solutions, where the peak is narrower and has a higher intensity. Although the broadness of this feature clearly changes under different conditions, the integrated area underneath the peak is similar indicating similar total electron density.

The electron density of such a sharp feature could originate from three possible sources, the adsorption of interfacial water, the adsorption of alkali ions, and electron density from ZrO_2 nanoparticles adsorbed at the surface. Past measurements[29] of the muscovite surface show adsorbed water layers located at 1.3 Å and 2.5 Å in the absence of adsorbing ions, with a shift of these layers away from the surface upon ion adsorption.[17, 33] We can directly probe the distribution of Rb^+, due to its conveniently located K edge at 15200 keV, though Rb^+ RAXR can be hampered by changes in the Rb^+ distribution with X-ray exposure. [34] We therefore minimized beam exposure during Rb^+ data collection to less than 1h from sample mounting to measurement completion, observing no instability. Nevertheless, minor effects of the X-ray beam may explain small incongruities between Rb^+ distribution and total electron density. Moreover, Rb^+ is a natural impurity in bulk muscovite, which may affect the determined Rb^+ distribution.

As shown in Fig. 3, Rb^+ is broadly distributed over the whole range of the Zr^{4+} distribution, up to ~19 Å above the substrate surface. In addition to the broad distribution there is a sharp peak at 1.9 Å, in reasonably good agreement with the sharp feature in the total electron density at 2.4 Å, and close to the previously determined location of the Rb^+ IS surface complex (1.9-2.0 Å).[17, 35] In addition, the Rb^+ surface coverage at the sharp peak resolved in this study (61±2%) is in excellent agreement with that presented in another CTR work (56±10%).[35] Not all of the total electron density at this position stems from Rb^+, however, as can be clearly seen in Fig. 3, which indicates an additional contribution to this feature. It appears reasonable that K^+ and Cs^+ exhibit similar distributions, since these ions all bind as IS complexes.[17, 31] The mixed contributions to this peak may explain why no systematic increase in electron density is observed when introducing the later alkali ions. Alternatively, the later alkali ions may exhibit lower surface coverages possibly due to their larger hydration shells,[16] and associated steric limitations in the presence of adsorbed ZrNP. The near constant electron density observed at ~2.4 Å, is then a compromise between higher number of electrons, associated surface coverage, and shifts in the other electron density contributions (water and ZrNP) to this feature. However, in LiCl and NaCl solutions, the first peak seen in the total electron density distribution is more likely to originate from the adsorption of interfacial water, because the hydrated Li^+ and Na^+ ions form an OS-binding mode at mica surface that displaces these ions further away from the surface.[17] The positions of the first two Rb peaks found in this work are similar to those reported previously[17] for the solution containing only RbCl, which indicates that those peaks are associated with surface adsorption, possibly in between ZrNP. Interestingly, the third Rb peak is not seen in RbCl-only solution, and is likely related to the ZrO_2 nanoparticle bound at surface.

The broad feature in all total electron density profiles represents the extension of adsorbed ZrO_2 nanoparticles, as clearly visualized by the RAXR-derived Zr^{4+} structure shown in Fig 3. The Zr^{4+} structure is similar for K^+, Rb^+, and Cs^+ solutions, with a vertical extension of ~ 16 Å and an average adsorption height of ~ 12 Å for ZrO_2 nanoparticles at mica surface. The vertical extension of the Zr distribution in Li^+ and Na^+ solutions grows to 23 Å, an increase of 44% compared to solutions of K^+, Rb^+ and Cs^+. A slight difference between Zr structures is seen in Li^+ and Na^+ solutions. The Zr structure in Li^+ solution is represented by a single broad Gaussian peak, whereas the Zr structure in Na^+ solution consist of one broad and intense peak and a much smaller peak at larger distance from the surface. Therefore, the average adsorption height in Li^+ solution is ~14 Å, 2 Å higher than that for Na^+ solution, which is similar to those for K^+, Rb^+ and Cs^+ solutions (~12 Å). This contributes to the difference in the shape of RAXR scans observed between Li^+ and the other solutions, as shown in Fig 2.

Table 1 Surface coverage of Zr^{4+} under different alkali ions

Alkali ions (0.1 M)	LiCl	NaCl	KCl	RbCl	CsCl
Surface coverage (Zr^{4+}/A_{UC})	3.7(1)	3.4(1)	3.1(1)	2.4(1)	1.8(1)

The results from RAXR analyses gave rise to the Zr surface coverage for different alkali solutions, as compiled in Table 1. The muscovite (001) surface has a constant negative charge of 1 e^-/A_{UC} [where A_{UC} is the area of the unit cell, A_{UC} = 46.72 Å² for muscovite (001), equivalent to 3.43 × 10^{-19} C/nm²], which is typically compensated by adsorbing cations. Instead of a coverage θ close to a charge compensating monolayer (θ_{CP} = 0.25 Zr^{4+}/A_{UC}), we find significantly higher Zr uptake in all cases (see Table 1). This increased uptake cannot be explained by "overcharging" which might be caused by highly charged Zr^{4+} ions,[36] but is rather indicative of the presence of Zr oligomers and their aggregation at the interface. The decrease of Zr surface coverage from LiCl to NaCl solution is small ($\Delta\theta_{Li\text{-}Na}$ = 0.3 Zr^{4+}/A_{UC}) almost within error range of both measurements, which is not the case for KCl, RbCl, and CsCl solutions, where a significant decrease of Zr surface coverage ($\Delta\theta_{K\text{-}Rb}$ = 0.7 Zr^{4+}/A_{UC}, $\Delta\theta_{Rb\text{-}Cs}$ = 0.6 Zr^{4+}/A_{UC}) is observed. This change in behavior with respect to the Zr surface coverage is probably related to two different competitive adsorption mechanisms between ZrO_2 nanoparticles and alkali ions at mica surface. These mechanisms will be discussed in section 2.4.

AFM results

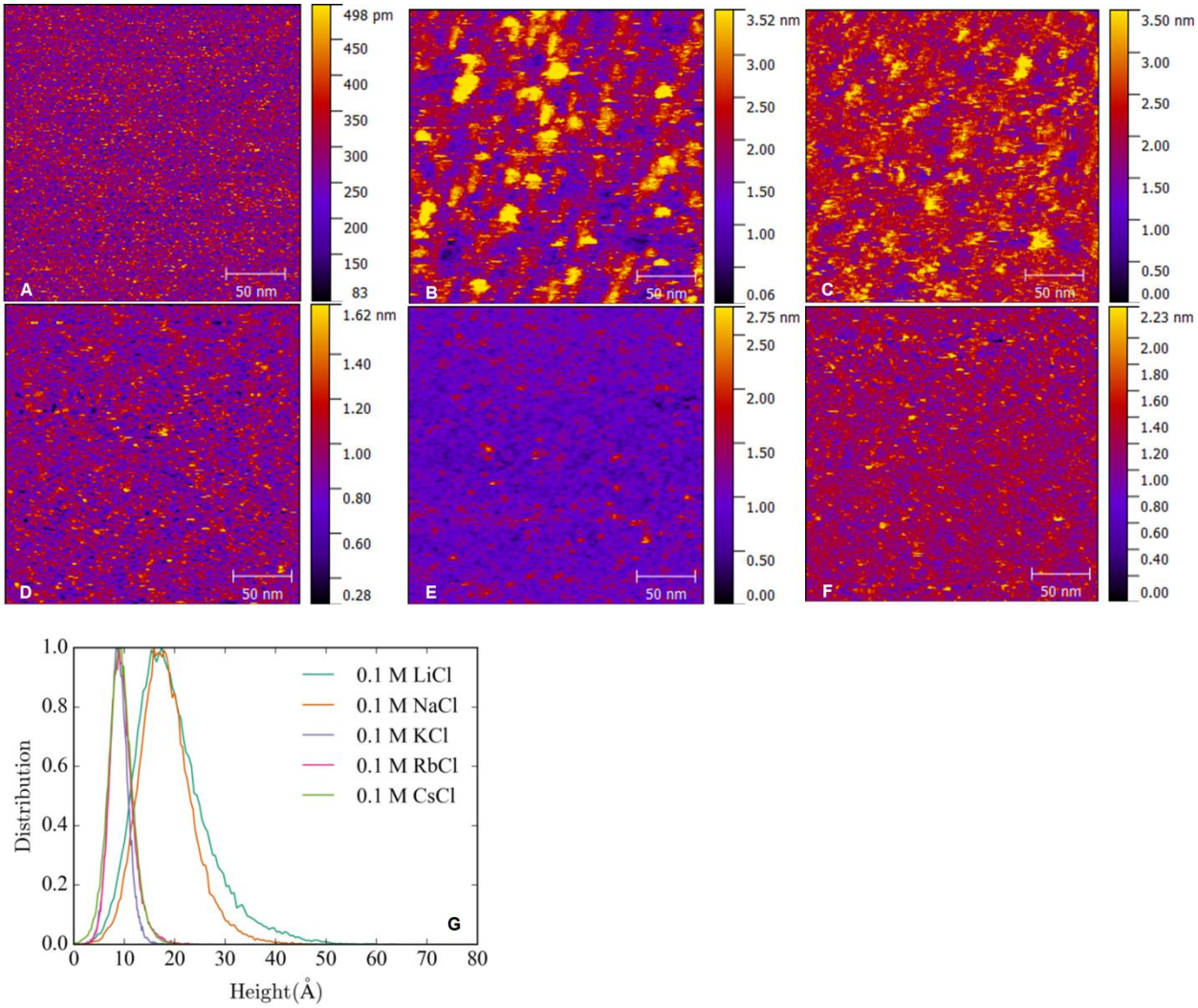

Figure 4. AFM images for mica surfaces reacted with Zr solution for 24 hrs with different alkali ion solutions including 0.1 M LiCl (B), 0.1 M NaCl (C), 0.1 M KCl (D), 0.1 M RbCl (E) and 0.1 M CsCl (F). Image A is a reference image collected in DI water. Each image has the same probing range of 250 × 250 nm² and the height color bar for each image is scaled differently for better comparison of dominant structure features. At the bottom (G), a height distribution analysis of five such micrographs is shown for each condition.

Fig 4 shows the AFM images collected under in situ condition for different Zr^{4+} samples containing five different alkali ions, including Li^+, Na^+, K^+, Rb^+, and Cs^+. In a 250 nm × 250 nm probing area, large nanoparticles of well-defined surface boundaries are clearly observed in LiCl solution. The average particle size is obtained from statistical analysis of >10 cross section profiles, arbitrarily drawn on each AFM image. As shown in Fig. S9, the lateral size of ZrO_2 nanoparticle in LiCl-containing solution is around 7.5(5) nm, which is slighter larger than that in NaCl solution with a lateral size of 6.5(5) nm. In NaCl solution, the surface morphology is determined by blurred features that lack well defined particle edges which are observed in LiCl solution. Despite the slight difference in the average lateral size of nanoparticles for LiCl and NaCl solutions, the vertical height distributions are similar with a peak centered at ~2 nm as

shown in Fig 4. The tail on the right side of the height distribution shift slightly towards higher values in LiCl solution compared to NaCl solution. This is in good agreement with the associated Zr distribution derived from RAXR shown in Fig. 3. In the other alkali solutions, the average lateral size of the adsorbed ZrO_2 nanoparticles is around 4.7(5) nm, significantly (~33%) smaller than that observed in LiCl and NaCl solutions, as clearly visible in Fig 4. The height distribution of ZrO_2 nanoparticles is also much narrower and centered at around 1 nm.

A qualitative comparison of nanoparticle sizes obtained from the analysis of AFM images results in two categories in terms of adsorbed ZrO_2 nanoparticles morphology, with relatively larger particles (both laterally and vertically) observed in LiCl and NaCl solutions and smaller nanoparticles in the other solutions. These two categories are consistent with the change of Zr surface coverage with the coexisting alkali ion type mentioned above. The reference zero for RAXR/CTR and AFM are different, the crystallographic zero is chosen to be the top layer oxygen and the AFM is chosen to be an arbitrarily "clean surface". As a consequence, the numerical values determined by the two methods will differ, but all observed trends and relative changes in dimensions agree well.

Competitive adsorption between ZrO_2 nanoparticles and alkali ions on a charged mineral surface

The muscovite (001) basal plane is negatively charged, and thus potentially reactive for binding both alkali cations and ZrO_2 nanoparticles. The question then arises, how ZrO_2 nanoparticles compete for surface sites with alkali ions at the charged surface. In the following discussion, we have excluded the H_3O^+ in the consideration of the competitive adsorption, even though it will participate in the sorption competition, since the influence of H_3O^+ is equivalent in all samples at constant solution pH. In this ternary system, the hydrated alkali ions adsorb on the mica surface as either IS or OS complexes depending on their hydration energy.[17] Adsorption of ZrO_2 nanoparticles seems to occur in a pseudo-"outer sphere" binding mode, where the surface of the nanoparticles is formed by (protonated) O rather than Zr.[18]

We will have to consider several energetic contributions to the exchange reaction: a) the energy required to desorb an adsorbed alkali ion (ΔG_{des}), b) the energy gained by adsorption of the ZrNP together with the energy gained by the rehydration of the surface site vacated IS complex (ΔG_{ads_NP}), c) the energy gained by rehydration of IS bound cations (ΔG_{hyd_i}).

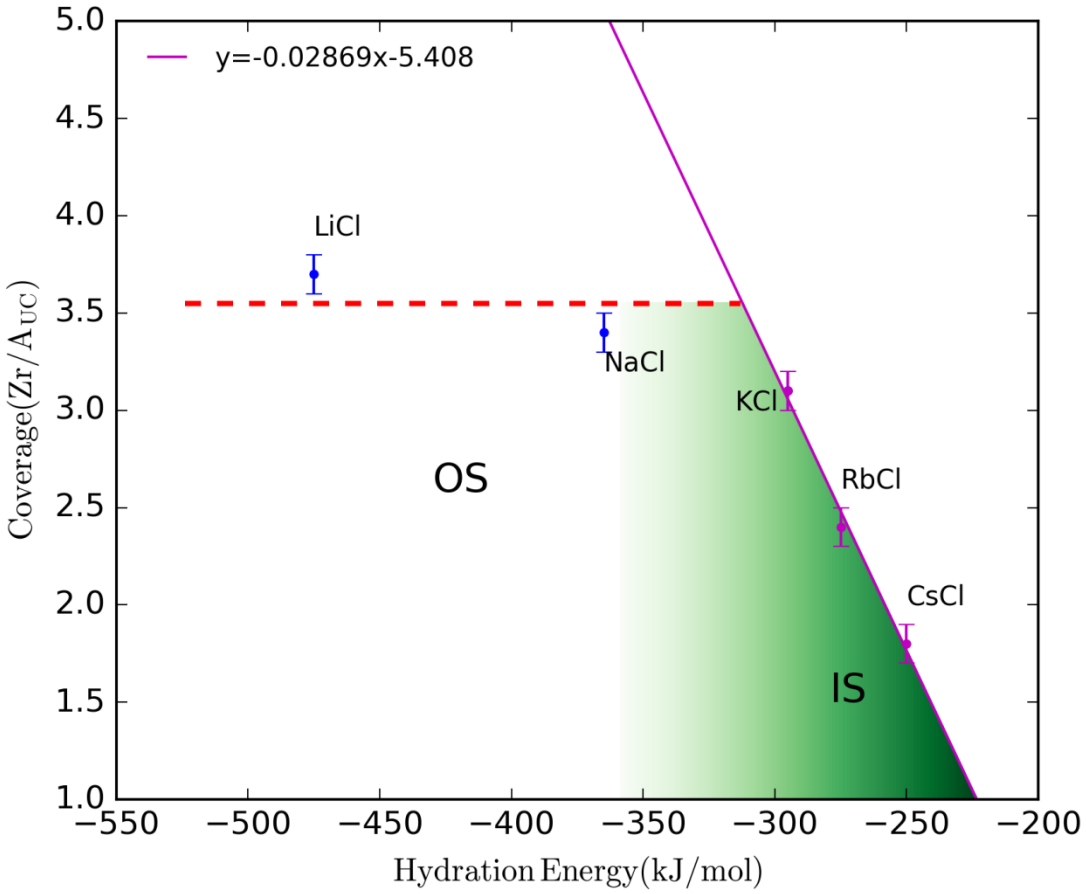

Figure 6. The relationship between Zr surface coverage [Zr] derived from RAXR modeling and the hydration energy ΔG_{hyd} of the associated coexisting alkali ions. The value of ΔG_{hyd} for each alkali ion is used from that reported by Marcus.[16] A linear trend line of [Zr] with ΔG_{hyd} is drawn for IS-bound ions (KCl, RbCl and CsCl). A horizontal dashed red line is drawn as an eye guide to show the small variation of [Zr] as a function of the type of OS-bound ions.

Competitive adsorption with OS-bound alkali ions (Li^+ and Na^+)

Outer sphere adsorbed alkali ions (Li^+ and Na^+) are registered ≥ 5 Å[17] above the substrate surface, due to space required to keep their hydration shells intact. The fully hydrated ions are relatively weakly bound at the substrate surface, and thus ZrO_2 nanoparticles can replace them on the surface easily. In this scenario, the size of ZrO_2 nanoparticles is unimportant, so that even large ZrO_2 nanoparticles can replace the loosely bound Li^+ and Na^+ OS complexes, despite their lower charge density. The AFM results (Fig. 4) confirm the presence of both large and small ZrO_2 nanoparticles at the mineral surface. Here, we can assume the particles' size distribution is mainly representative of their aggregation behavior in solution.[18] Such a 'nonselective' adsorption of ZrO_2 nanoparticle in both Li^+ and Na^+ solutions is also inferred by the weak correlation between the Zr surface coverage and the associated hydration energy of coexisting ions (Li^+ and Na^+), as shown in Fig 6. The interfacial exchange reaction is independent of the

ions' hydration energy, because the desorption reaction does not involve changes in their hydration spheres, but rather is a substitution reaction between two types of "OS"-bound chemical entities. As ZrNP of any size will have a significantly higher charge than the A^+ alkali cations, the exchange of A^+ by ZrNP will always be favorable, due to the corresponding difference in $\Delta G_{des}(A^+)$ and ΔG_{ads_NP}(ZrNP).

A simplified energetic comparison based on purely electrostatic considerations (See SI for details) shows that particles in the size range of V = 20× (65 ~ 75)^2 Å^3 have an adsorption energy due to electrostatic attraction in the range of the adsorption energy of hydrated Li^+ and Na^+ reported by Lee et al. [-(13-17) kJ/mol].[37] This size is in very good agreement with the nanoparticles observed in our study, suggesting that electrostatic terms dominate the reaction energetically, as previously shown for the adsorption of ions on the same surface. [38]

Competitive adsorption with IS-bound alkali ions (K^+, Rb^+ and Cs^+)

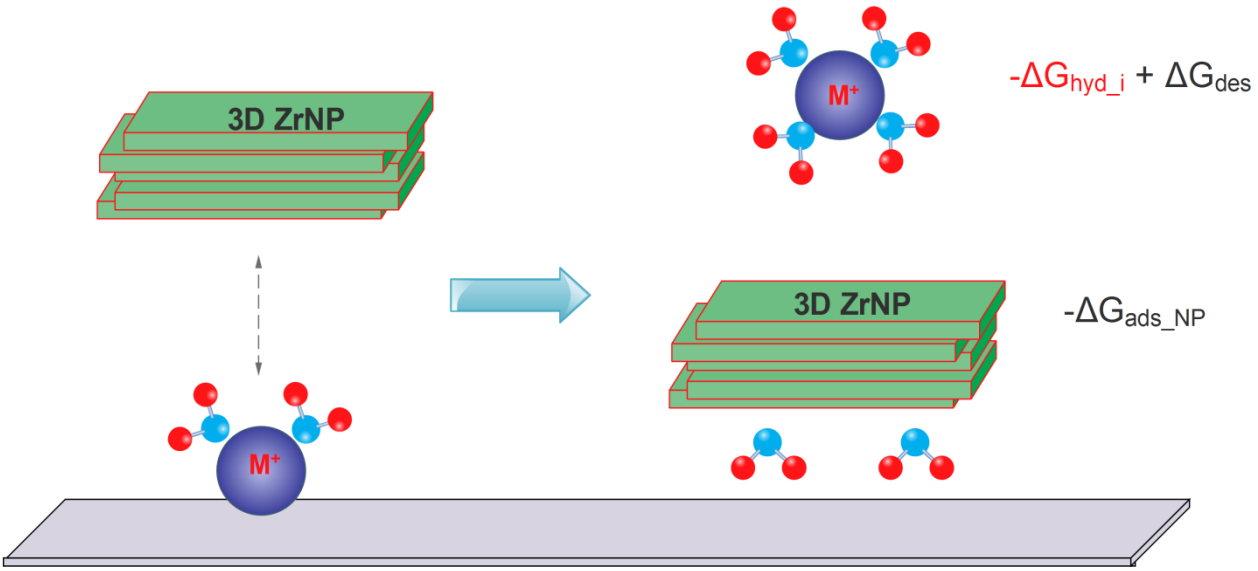

Figure 7. Schematic diagram of the competitive adsorption of ZrO_2 nanoparticles with IS-bound alkali ions on mica surface. In the process of the competitive adsorption, energy terms for different chemistry steps are labeled, including energy cost for the desorption of bound IS ion (ΔG_{des}), energy gain for rehydration of the dissociated alkali ion ($-\Delta G_{hyd\_i}$), and the binding of ZrO_2 nanoparticle via an electrostatic attraction ($-\Delta G_{ads\_NP}$). The energy terms highlighted in red are only associated with solutions containing IS-bound ions, while the other energy terms are shared by all alkali solutions.

The heavier alkali ions, K^+, Rb^+ and Cs^+, are relatively larger in size than Li^+ and Na^+, leading to smaller charge density and weaker hydration.[16] As a result, when these hydrated alkali ions approach the mica surface, they replace part of their hydration shell with surface functional groups to form IS complexes. Alkali ions with such an IS binding mode have larger adsorption energies compared to OS-bound ions (Li^+ and Na^+). However, due to the necessary dehydration of the ions their adsorption energy will depend directly on their hydration energy, as part of it will have to be expended in the dehydration process. Nevertheless, in this IS binding mode, the energy cost for replacing the partially hydrated alkali ions registered at the substrate surface by ZrO_2 nanoparticles is a larger factor in the process of the competitive adsorption.

Smaller ZrO_2 nanoparticles, bearing higher charge density, are more competitive to replace IS-bound alkali ions. This becomes evident in the slightly smaller vertical size determined by RAXR, and is confirmed in the AFM images (Fig. 4), where smaller ZrO_2 nanoparticles (32% smaller laterally) are observed in solutions containing IS adsorbed ions (K^+, Rb^+, and Cs^+) compared to the case of OS-bound ions. Once again this size compares well with electrostatic calculations that predict ZrNP with a size of $V = 17.5 \times (52 \sim 56)^2$ $Å^3$ should exhibit similar adsorption energies as the heavier alkali cations [-(21-23) kJ/mol].[37]

We found that the Zr surface coverage displays a strong linear relationship with the hydration energy of the coexisting alkali ions as illustrated in Fig. 6. To understand the observed linear relationship between Zr coverage and hydration energy of coexisting alkali ions, we identify the energy terms in this chemical process. As illustrated in Fig.7, in this ternary system that contains IS-bound ions and ZrO_2 nanoparticles as well as the mineral surface, we have to consider not only the energy terms for ad- and desorption (ΔG_{ads_NP}(ZrNP) and $\Delta G_{des}(A^+)$, respectively), but also the effects of hydration of ions and surface. The energy gain relating to the rehydration of the partially hydrated IS complexes when releasing from the substrate surface, is directly related to their hydration energy. If we consider that approximately half their hydration shell remains, when IS bound to the substrate surface, the energy gain is equivalent to around half of its hydration energy. The energy term originating from the rehydration of dissociated IS ions may be the dominant term among all energy terms,[16, 37] which explains the linear relationship between the Zr surface coverage and the hydration energy of coexisting alkali ions. Thus, the energetic favorability of the alkali ions' desorption acts as a chemical selector in preference of smaller NP with high charge density over their larger counterparts.

Conclusions

In this work, the sorption behavior of ZrO_2 nanoparticles on muscovite (001) surface was studied in the presence of different alkali ions. Combining X-ray surface scattering with AFM imaging, we found the binding mode of alkali ions at the muscovite surface plays a critical role in determining size and quantity of the sorption of ZrO_2 nanoparticles. OS-bound ions (Li^+ and Na^+) are weakly associated with the mineral surface and are thus easily replaced by ZrO_2 nanoparticles of any size, due to the ZrO_2 nanoparticles' high charge density. The size distribution at the surface is then representative of the distribution in solution. On the contrary, the IS-bound ions (K^+, Rb^+, and Cs^+) are more competitive for the adsorption of ZrO_2 nanoparticles, so that it is only energetically favorable to replace IS bound alkali ions for particles of smaller size and higher charge density are.

The relationship between Zr surface coverage (θ_{Zr}) and the hydration energy (ΔG_{hyd_i}) of the competing alkali ion changes with the binding mode of alkali ions. For OS-bound alkali ions no significant correlation between θ_{Zr} and ΔG_{hyd_i} is observed, because the substitution of one OS-bound species for another does not involve hydration reactions. On the other hand, a strong linear relationship between θ_{Zr} and ΔG_{hyd_i} is observed for the adsorption of ZrO_2 nanoparticles in the presence of IS-bound alkali ions, which is related to the rehydration of desorbed alkali ions, and

the dependence of these ions' adsorption energy on the same parameter. The linear relationship suggests this energetic contribution dominates the total reaction energy.

This work was in part motivated by previous work in our group that revealed unusual observations regarding the sorption behavior of Th^{4+} on the same mica (001) surface.[15] Here, the highest uptake was observed in the presence of Li^+, like in this study, but followed by K^+, with the lowest uptake in the presence of Na^+. No such behavior was found here, which demonstrates that other effects must be taken into consideration for explaining Th^{4+}'s behavior, and calls into question the often used analogy between Zr^{4+} and tetravalent actinides (e.g. Th^{4+}, U^{4+}, or Pu^{4+}). However, it should be noted that the fundamental relationship between competitive adsorption of nanoparticles and hydration energy and binding mode of the alkali cation would be expected for Th^{4+}, but are apparently not sufficient to explain its unusual sorption behavior.

Our work demonstrates that the chemical composition of the aqueous solution affects the interfacial chemistry of charged nanoparticles in a more complicated way than expected. The effect of alkali ions on ZrO_2 nanoparticle sorption suggest that even "simple" alkali ions cannot always be considered as uninvolved 'spectator' ions that are chemically indistinct from each other. Understanding all energetic contributions and the possible differences in e.g. hydration energy is essential for an accurate description of surface processes of environmentally relevant species.

Acknowledgements

This study is funded by Helmholtz Young Investigator Group "Structures and reactivity at the aqueous/mineral interface" (VH-NG-942).The X-ray data were collected at the Rossendorf Beamline at the ESRF (ROBL, BM-20) and GeoSoilEnviroCARS (The University of Chicago, Sector 13), Advanced Photon Source (APS), Argonne National Laboratory. GeoSoilEnviroCARS is supported by the National Science Foundation - Earth Sciences (EAR - 1634415) and Department of Energy- GeoSciences (DE-FG02-94ER14466). This research used resources of the Advanced Photon Source, a U.S. Department of Energy (DOE) Office of Science User Facility operated for the DOE Office of Science by Argonne National Laboratory under Contract No. DE-AC02-06CH11357. The model refinement is performed using computation resource provided by Department of Information Services and Computing in Helmholtz-Zentrum Dresden – Rossendorf. We also thank A. Panzarella of the AFM Platform of the Partnership for Soft Condensed Matter (PSCM) of the ESRF for assisting with the AFM measurements.

Supporting Information. XR/RAXR modeling approach; electrostatic energy calculations; XR experimental setup; complete RAXR datasets and fits; AFM profiles; XR fitting result summary.

References

1. Li, Y.; Wang, H.; Xie, L.; Liang, Y.; Hong, G.; Dai, H., MoS2 nanoparticles grown on graphene: an advanced catalyst for the hydrogen evolution reaction. *Journal of the American Chemical Society* **2011,** *133*, (19), 7296-7299.
2. Niemeyer, C. M., Nanoparticles, Proteins, and Nucleic Acids: Biotechnology Meets Materials Science. *Angewandte Chemie International Edition* **2001,** *40*, (22), 4128-4158.
3. Aricò, A. S.; Bruce, P.; Scrosati, B.; Tarascon, J.-M.; van Schalkwijk, W., Nanostructured materials for advanced energy conversion and storage devices. *Nature Materials* **2005,** *4*, 366.
4. Wang, P.; Abrusci, A.; Wong, H. M.; Svensson, M.; Andersson, M. R.; Greenham, N. C., Photoinduced charge transfer and efficient solar energy conversion in a blend of a red polyfluorene copolymer with CdSe nanoparticles. *Nano letters* **2006,** *6*, (8), 1789-1793.
5. Veiseh, O.; Gunn, J. W.; Zhang, M., Design and fabrication of magnetic nanoparticles for targeted drug delivery and imaging. *Advanced drug delivery reviews* **2010,** *62*, (3), 284-304.
6. Meng, H.; Liong, M.; Xia, T.; Li, Z.; Ji, Z.; Zink, J. I.; Nel, A. E., Engineered design of mesoporous silica nanoparticles to deliver doxorubicin and P-glycoprotein siRNA to overcome drug resistance in a cancer cell line. *ACS nano* **2010,** *4*, (8), 4539-4550.
7. Waychunas, G. A.; Kim, C. S.; Banfield, J. F., Nanoparticulate iron oxide minerals in soils and sediments: unique properties and contaminant scavenging mechanisms. *Journal of nanoparticle research* **2005,** *7*, (4-5), 409-433.
8. Acosta, E., Bioavailability of nanoparticles in nutrient and nutraceutical delivery. *Current opinion in colloid & interface science* **2009,** *14*, (1), 3-15.
9. Schymura, S.; Fricke, T.; Hildebrand, H.; Franke, K., Elucidating the Role of Dissolution in CeO2 Nanoparticle Plant Uptake by Smart Radiolabeling. *Angewandte Chemie International Edition* **2017,** *56*, (26), 7411-7414.
10. Schwabe, F.; Schulin, R.; Rupper, P.; Rotzetter, A.; Stark, W.; Nowack, B., Dissolution and transformation of cerium oxide nanoparticles in plant growth media. *Journal of nanoparticle research* **2014,** *16*, (10), 2668.
11. Novikov, A. P.; Kalmykov, S. N.; Utsunomiya, S.; Ewing, R. C.; Horreard, F.; Merkulov, A.; Clark, S. B.; Tkachev, V. V.; Myasoedov, B. F., Colloid transport of plutonium in the far-field of the Mayak Production Association, Russia. *Science* **2006,** *314*, (5799), 638-641.
12. Kersting, A.; Efurd, D.; Finnegan, D.; Rokop, D.; Smith, D.; Thompson, J., Migration of plutonium in ground water at the Nevada Test Site. *Nature* **1999,** *397*, (6714), 56.
13. Geckeis, H.; Lützenkirchen, J.; Polly, R.; Rabung, T.; Schmidt, M., Mineral–water interface reactions of actinides. *Chemical reviews* **2013,** *113*, (2), 1016-1062.
14. Schmidt, M.; Wilson, R. E.; Lee, S. S.; Soderholm, L.; Fenter, P., Adsorption of plutonium oxide nanoparticles. *Langmuir* **2012,** *28*, 2620-2627.
15. Schmidt, M.; Hellebrandt, S.; Knope, K. E.; Lee, S. S.; Stubbs, J. E.; Eng, P. J.; Soderholm, L.; Fenter, P., Effects of the background electrolyte on Th(IV) sorption to muscovite mica. *Geochimica et Cosmochimica Acta* **2015,** *165*, 280-293.
16. Marcus, Y., Thermodynamics of solvation of ions. Part 5.—Gibbs free energy of hydration at 298.15 K. *Journal of the Chemical Society, Faraday Transactions* **1991,** *87*, (18), 2995-2999.
17. Lee, S. S.; Fenter, P.; Nagy, K. L.; Sturchio, N. C., Monovalent ion adsorption at the muscovite (001) - solution interface: Relationships among ion coverage and speciation, interfacial water structure, and substrate relaxation. *Langmuir* **2012,** *28*, 8637-8650.
18. Qiu, C.; Eng, P. J.; Hennig, C.; Schmidt, M., Formation and Aggregation of ZrO2 Nanoparticles on Muscovite (001). *The Journal of Physical Chemistry C* **2018,** *122*, (7), 3865-3874.
19. Israelachvili, J.; Wennerstrom, H., Role of hydration and water structure in biological and colloidal interactions. *Nature* **1996,** *379*, (6562), 219-225.
20. Pashley, R., DLVO and hydration forces between mica surfaces in Li+, Na+, K+, and Cs+ electrolyte solutions: A correlation of double-layer and hydration forces with surface cation exchange properties. *Journal of Colloid and Interface Science* **1981,** *83*, (2), 531-546.
21. Pashley, R., Hydration forces between mica surfaces in electrolyte solutions. *Advances in Colloid and Interface Science* **1982,** *16*, (1), 57-62.

22. Eikenberry, E. F.; Brönnimann, C.; Hülsen, G.; Toyokawa, H.; Horisberger, R.; Schmitt, B.; Schulze-Briese, C.; Tomizaki, T., PILATUS: a two-dimensional X-ray detector for macromolecular crystallography. *Nucl. Inst. Meth. Phys. Res. A* **2003,** *501*, (1), 260-266.
23. Cross, J. O.; Newville, M.; Rehr, J. J.; Sorensen, L. B.; Bouldin, C. E.; Watson, G.; Gouder, T.; Lander, G. H.; Bell, M. I., Inclusion of local structure effects in theoretical x-ray resonant scattering amplitudes using ab initio x-ray-absorption spectra calculations. *Phys. Rev. B* **1998,** *58*, (17), 11215.
24. Nečas, D.; Klapetek, P., Gwyddion: an open-source software for SPM data analysis. *Open Physics* **2012,** *10*, (1), 181-188.
25. Fenter, P., X-ray Reflectivity as a Probe of Mineral-Fluid Interfaces: A User Guide. *Rev. Min. Geochem.* **2002,** *49*, 149-220.
26. Robinson, I. K., Crystal truncation rods and surface roughness. *Phys. Rev. B* **1986,** *33*, (6), 3830-3836.
27. Robinson, I. K.; Tweet, D. J., Surface X-ray-Diffraction. *Rep. Prog. Phys.* **1992,** *55*, (5), 599-651.
28. Park, C.; Fenter, P., Phasing of Resonant Anomalous X-ray Reflectivity Spectra and Direct Fourier Synthesis of Element-Specific Partial Structures at Buried Interfaces. *J. Appl. Crystallogr.* **2007,** *40*, (2), 290-301.
29. Cheng, L.; Fenter, P.; Nagy, K. L.; Schlegel, M. L.; Sturchio, N. C., Molecular-Scale Density Oscillations in Water Adjacent to a Mica Surface. *Phys. Rev. Lett.* **2001,** *87*, (15), 156103.
30. Schlegel, M. L.; Nagy, K. L.; Fenter, P.; Cheng, L.; Sturchio, N. C.; Jacobsen, S. D., Cation sorption on the muscovite (001) surface in chloride solutions using high-resolution X-ray reflectivity. *Geochimica et Cosmochimica Acta* **2006,** *70*, (14), 3549-3565.
31. Brugman, S. J. T.; Townsend, E. R.; Smets, M. M. H.; Accordini, P.; Vlieg, E., Concentration-Dependent Adsorption of CsI at the Muscovite–Electrolyte Interface. *Langmuir* **2018,** *34*, (13), 3821-3826.
32. Park, C.; Fenter, P. A.; Sturchio, N. C.; Nagy, K. L., Thermodynamics, Interfacial Structure, and pH Hysteresis of Rb+ and Sr2+ Adsorption at the Muscovite (001)−Solution Interface. *Langmuir* **2008,** *24*, (24), 13993-14004.
33. Schmidt, M.; Lee, S. S.; Wilson, R. E.; Soderholm, L.; Fenter, P., Sorption of tetravalent Thorium on Muscovite. *Geochim. Cosmochim. Acta* **2012,** *88*, 66-76.
34. Lee, S. S.; Fenter, P.; Nagy, K. L.; Sturchio, N. C., Monovalent Ion Adsorption at the Muscovite (001)–Solution Interface: Relationships among Ion Coverage and Speciation, Interfacial Water Structure, and Substrate Relaxation. *Langmuir* **2012,** *28*, (23), 8637-8650.
35. Pintea, S.; de Poel, W.; de Jong, A. E. F.; Vonk, V.; van der Asdonk, P.; Drnec, J.; Balmes, O.; Isern, H.; Dufrane, T.; Felici, R.; Vlieg, E., Solid–Liquid Interface Structure of Muscovite Mica in CsCl and RbBr Solutions. *Langmuir* **2016,** *32*, (49), 12955-12965.
36. Lee, S. S.; Schmidt, M.; Laanait, N.; Sturchio, N. C.; Fenter, P., Investigation of Structure, Adsorption Free Energy, and Overcharging Behavior of Trivalent Yttrium Adsorbed at the Muscovite (001)–Water Interface. *J. Phys. Chem. C* **2013,** *117*, (45), 23738-23749.
37. Lee, S. S.; Fenter, P.; Nagy, K. L.; Sturchio, N. C., Changes in adsorption free energy and speciation during competitive adsorption between monovalent cations at the muscovite (001)-water interface. *Geochimica et Cosmochimica Acta* **2013,** *123*, 416-426.
38. Park, C.; Fenter, P. A.; Nagy, K. L.; Sturchio, N. C., Hydration and Distribution of Ions at the Mica-Water Interface. *Phys. Rev. Lett.* **2006,** *97*, (1), 016101.

Supporting Information for the manuscript

Competitive adsorption of ZrO_2 nanoparticle and alkali cations (Li^+ – Cs^+) on muscovite (001)

Canrong Qiu,[1] Peter J. Eng,[2] Christoph Hennig,[1] Moritz Schmidt[1,*]

[1] Helmholtz-Zentrum Dresden-Rossendorf, Institute of Resource Ecology, Dresden, Germany

[2] Center for Advanced Radiation Sources, University of Chicago, Chicago, IL 60637, USA

[*]Corresponding author: Tel. : +49 351 260 3136; E-mail address: moritz.schmidt@hzdr.de

Contents:

XR/RAXR modeling approach; electrostatic energy calculations; XR experimental setup; complete RAXR datasets and fits; AFM profiles; XR fitting result summary.

15 pages, 9 figures, and 1 table.

1. CTR/RAXR modeling strategy

CTR data were fit by a parameterized electron density model consisting of three components: the substrate, the interface, and bulk water. The interface comprises relaxed surface layers of muscovite and any adsorbed species. The reflectivity R(q) of a given model is then calculated as

$$R(q) = \left(\frac{4\pi r_e}{qA_{UC}}\right)^2 |F_{UC} \cdot F_{CTR} + F_{int} + F_W|^2,$$

where q is the momentum transfer, $r_e = 2.818 \times 10^{-5}$Å is the classical electron radius, and A_{UC} is the area of the unit cell in the *ab* plane ($A_{UC} = 46.72$Å^2). Each F is a structure factor (unit cell, CTR, interface, and bulk water, respectively) defined as $F = \sum_j c_j f_j(q) exp(iqz_j) exp[-(qu_j)^2/2]$, where $f_j(q)$ is the atomic scattering factor with the expression summed over all atoms within the substructure of interest and c_j, u_j, and z_j are the occupancy, rms distribution width and distance from the muscovite surface of atom j, respectively. Each structure factor represents one of the components listed above. The unit cell form factor, F_{UC}, is calculated based on atom positions calculated from XRD data [2] and is multiplied by the CTR form factor, $F_{CTR} = 1/[1 - exp(-iqd/4)]$ [3], where d is the muscovite (001) spacing (= 19.97 ± 0.02 Å) [2], to account for the semi-infinite distribution of substrate layers.

Atoms within the top two unit-cells from the surface were allowed to relax from their ideal positions in the bulk crystal to yield best-fit results [2, 4]. Typically, each adsorbed species is described as a Gaussian distribution by the three parameters: occupancy c, distance from the muscovite surface z, and distribution width u. The distribution of water above the actual sorption structure is described by a layered-water model [2, 5]. This model consists of a series of equally-spaced Gaussian peaks with the average electron density of bulk water (0.33e$^-$/Å^3). Only the distance of the first water layer from the surface, z_W, and its width, u_W (as distribution width of the first Gaussian) are fit, giving the profile an error function shape in the region of interest.

Several models applying varying starting conditions were tested to validate the reliability of the best-fit model. The least-squares fitting procedure yields the statistical uncertainty for each fitting parameter. Each fitting result is evaluated by a scaled χ^2 value according to

$$\chi^2 = \left[\sum_k (I_k - I_{calc,k})^2/\sigma_k^2\right]/(N - N_p) \qquad \text{(S1)}$$

where N and N_p are the numbers of data points and parameters used in the model-fit, respectively, I_k and σ_k are the intensity and the uncertainty of the kth data point, respectively, and I_{calc} is the intensity calculated for the particular set of parameters from the model [3]. The R factor (eq. S2) of the best fit is also reported for comparison.

$$R = \sum_k (|I_k - I_{calc,k}|/I_k)/N \qquad \text{(S2)}$$

The parameterized RAXR model is build up from the same components used in the CTR data fitting: Gaussian distributions described by occupancy c_j, distribution width u_j, and distance from the muscovite surface z_j. For the RAXR model, this is calculated for the partial structure factor that includes only the resonant atom (in this case, Zr). A model consisting of one Gaussian peak was found to result in the best fit for Zr-mica samples in solutions containing LiCl, KCl, RbCl

and CsCl, while a model of two Gaussian peaks is necessary to fit Zr-mica sample in NaCl solution, and the parameters are summarized in Table S1.

2. Calculation of the electrostatic adsorption energy of ZrO_2 nanoparticles

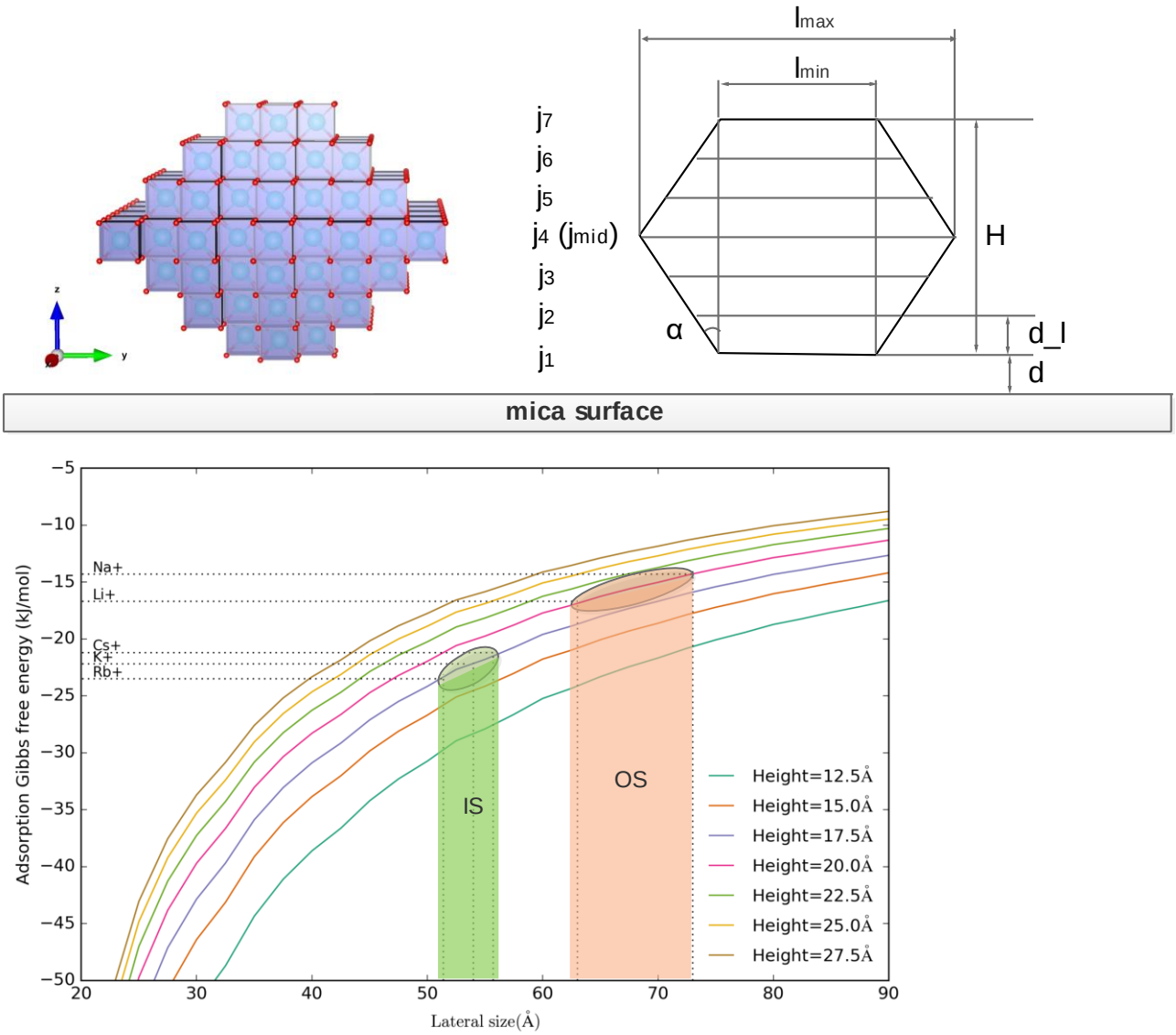

Figure S1 (Top) Geometrical model for the calculation of electrostatic potential energy based on the assumption of ellipsoid-like ZrO_2 nanoparticles containing layer-plates, as illustrated from a representative molecule structure shown on the left. The geometrical model shown on the top right is drawn based on the ellipsoid-like structure being projected on a plane defined by **y** and **z** axis. (Bottom) The variation of the adsorption free energy of nanoparticles as a function of lateral and vertical sizes.

We performed the calculation of the adsorption free energy for nanoparticles of lateral size ranging from 20 Å to 90 Å and vertical size ranging from 12.5 Å to 27.5 Å. The size ranges used

in the calculation cover the associated size range obtained from AFM and RAXR results, as discussed in the main text. The adsorption Gibbs free energy for alkali ions are highlighted in this figure as dash lines according to values reported by Lee et al.[10] The calculations presented here, and described in detail below, are based on a number of assumptions which appear plausible, but are not verified by our experimental data. As such, the numerical results cannot be interpreted as exact adsorption energies of such particles. The resulting agreement between calculated and experimentally derived particle sizes is nonetheless interesting. Examples of assumptions are the shape and morphology of the nanoparticles, as well as their internal structure. We also do not consider any chemical bonding between the nanoparticles and the surface, and the good agreement with experimental data suggests chemical bonding may indeed play a minor role in the nanoparticle adsorption process.

The electrostatic potential energy (ΔG_{elec}) of ZrO2 nanoparticles bounded at muscovite (001) surface can be calculated if we make an assumption of ZrO_2 nanoparticle bearing an ellipsoid shape, which contains interconnected nanosheet structure with an inter-layer spacing of 2.5 Å, as shown in Fig.S1 (left). The net surface charges come from the protonation of surface O groups at each layer edge. The protons bonding to surface O groups are assumed to have same heights as the associated structural layer. The size effect of protons is ignored, and thus each proton is simply treated as a point charge. As a result, the protons at the same structural layer are indistinct from each other to generate electrostatic potential energy. At pH 2.5, we assume terminal O groups are doubly protonated. For cubic structural unit of ZrO_2 nanoparticle, the charge density at nanoparticle edges is approximated to 2 e^+/2.5 Å (e^+ is one positive charge). At this surface charge density, the total number of positive charges at each structural layer could be calculated knowing the associated edge length L (assuming a square lateral shape for simplicity). A single point charge at Layer-j with a layer height of h_{Lj} is equivalent to the reference ΔG_{elec} ($\Delta G_{elec,\ ref}$) corrected by an energy offset ($\Delta G_{elec,\ offset}$) caused by the height difference (Δh) compared to the reference height (h_{ref}). The $\Delta G_{elec,\ offset}$ is calculated from the electrostatic potential gradient ($d\Delta G_{elec}/dh$) and the associated height difference Δ h. The electrostatic field (E) is created at mica surface from the structural permanent charge, and the value of E decreases with the distance from the substrate surface. The value of $d\Delta G_{elec}/dh$ represents the rate of change of the electrostatic field E with the height. In summary, to calculate the total ΔG_{elec} of an ellipsoid-like ZrO_2 nanoparticles, we make following assumptions:

1. The inter-layer spacing is 2.5 Å.
2. Each layer bears a square shape with the edge length of L.
3. The net surface charge density equals 2 e^+/2.5 Å at layer edges.
4. The reference height is set to 2.5 Å above the substrate surface.
5. The value of reference ΔG_{elec} equals -16.7 kJ/mol, which is based on the Gibbs free energy of Li^+ on muscovite (001) surface determined by Lee et al. [10]
6. The nanoparticle bears an aspect ratio, which is determined by the lateral size defined by the longest edge length (L_{max}) and the vertical length of nanoparticles (H).

Using these assumptions, the total Gibbs free energy of an adsorbed ZrO_2 nanoparticle can be expressed by the following equation:

$$\Delta G_{total} = \frac{\sum_{j=1}^{j=n_l} N_j \left(\Delta G_{elec,ref} + \sum_{k=1}^{k=j-1} \Delta h_k \times \frac{\partial \Delta G_{elec,k}}{\partial h_k} \right)}{\frac{l_{max} \times l_{max}}{A_{UC}}} \quad \text{(S3)},$$

where $\Delta G_{elec,ref}$ is the reference equaling -16.7 kJ/mol, Δh_k is the inter-layer spacing equaling 2.5 Å, $\frac{\partial \Delta G_{elec,k}}{\partial h_k}$ represents the electrostatic potential gradient at Layer-k, N_j is the total number of net positive charge at Layer-j, A_{UC} is the surface area of one unit cell of muscovite (001) equaling 46.72 $Å^2$. To calculate the energy offset $\Delta G_{elec,\,offset}$ for a point charge at Layer-j, we apply the discrete integration to account for all underneath layers, which is expressed as $\sum_{k=1}^{k=j-1} \Delta h_k \times \frac{\partial \Delta G_{elec,k}}{\partial h_k}$ as also shown in equation (1). To account for the decreasing of electrostatic potential gradient with layer height, the value of electrostatic potential gradient at Layer-k is described as

$$\frac{\partial \Delta G_{elec,k}}{\partial h_k} = \frac{\partial \Delta G_{elec,1}}{\partial h_1} \times e^{-f(k-1)} \quad \text{(S4)},$$

where $\frac{\partial \Delta G_{elec,1}}{\partial h_1}$ is the electrostatic potential gradient at the first layer using a value of 2.4 kJ/mol given by Lee et al.[10], k is the layer number, and *f* is the damping factor given arbitrarily as 0.2. We can relate the charge number N_j at Layer-j to the geometry of the nanoparticle as follows,

$$N_{j(j \le j_{mid})} = \frac{[2 \times \Delta z_j \times \tan\alpha + l_{min}] \times 4}{2.5} \quad \text{(S5), and}$$

$$N_{j(j > j_{mid})} = \frac{[l_{max} - 2 \times \Delta z_j \times \tan\alpha] \times 4}{2.5} \quad \text{(S6)},$$

for layers lower than the middle layer (Layer-j_{mid}) and layers higher than the middle layer, respectively. In the equation (3) and equation (4), Δz_j represents interlayer spacing equaling 2.5 Å, and the angle α is the aspect angle shown in Fig.S1. The aspect angle can be defined based on

$$\tan\alpha = \frac{l_{max} - l_{min}}{H} \quad \text{(S7)}$$

With these definitions, we can calculate the value of the total Gibbs free energy for the adsorption of any ZrO_2 nanoparticle solely from its dimension, which is defined by its lateral size (L_{max}) as well as its vertical size (H). We performed a series of calculations to obtain energy profiles, which depict the sorption energy variation of a nanoparticle with both the lateral and vertical sizes, as illustrated in Fig S1 (bottom). The calculated adsorption energies are approximate values and cannot be considered true adsorption Gibbs' free energies, but may serve as an indicator for the driving force behind the size selection observed in our experiments. Additional studies on a better-developed mathematical basis, e.g. including molecular dynamics simulations, may become fruitful.

3. Experimental setup for X-ray experiments

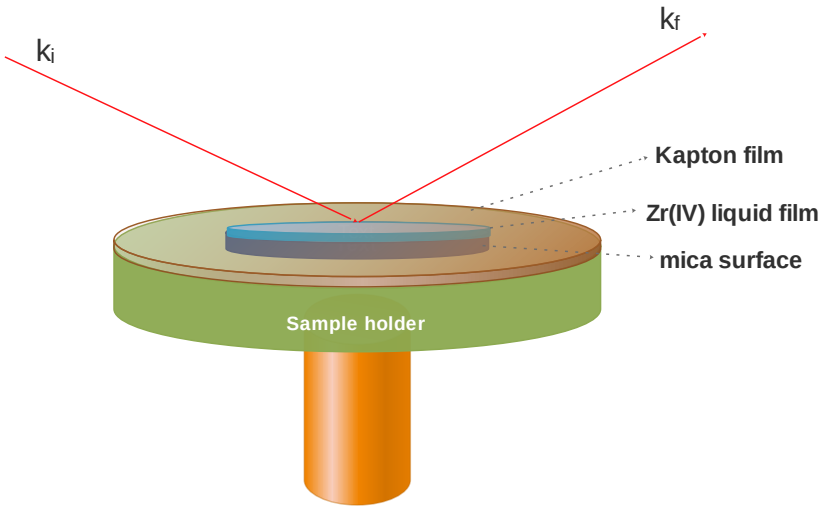

Figure S2. Sample cell for the X-ray reflectivity experiments [1]. The sample is fixed with a Kapton window that also traps and maintains a thin liquid film on top of the mineral surface during X-ray reflectivity measurement.

4. RAXR data and fits

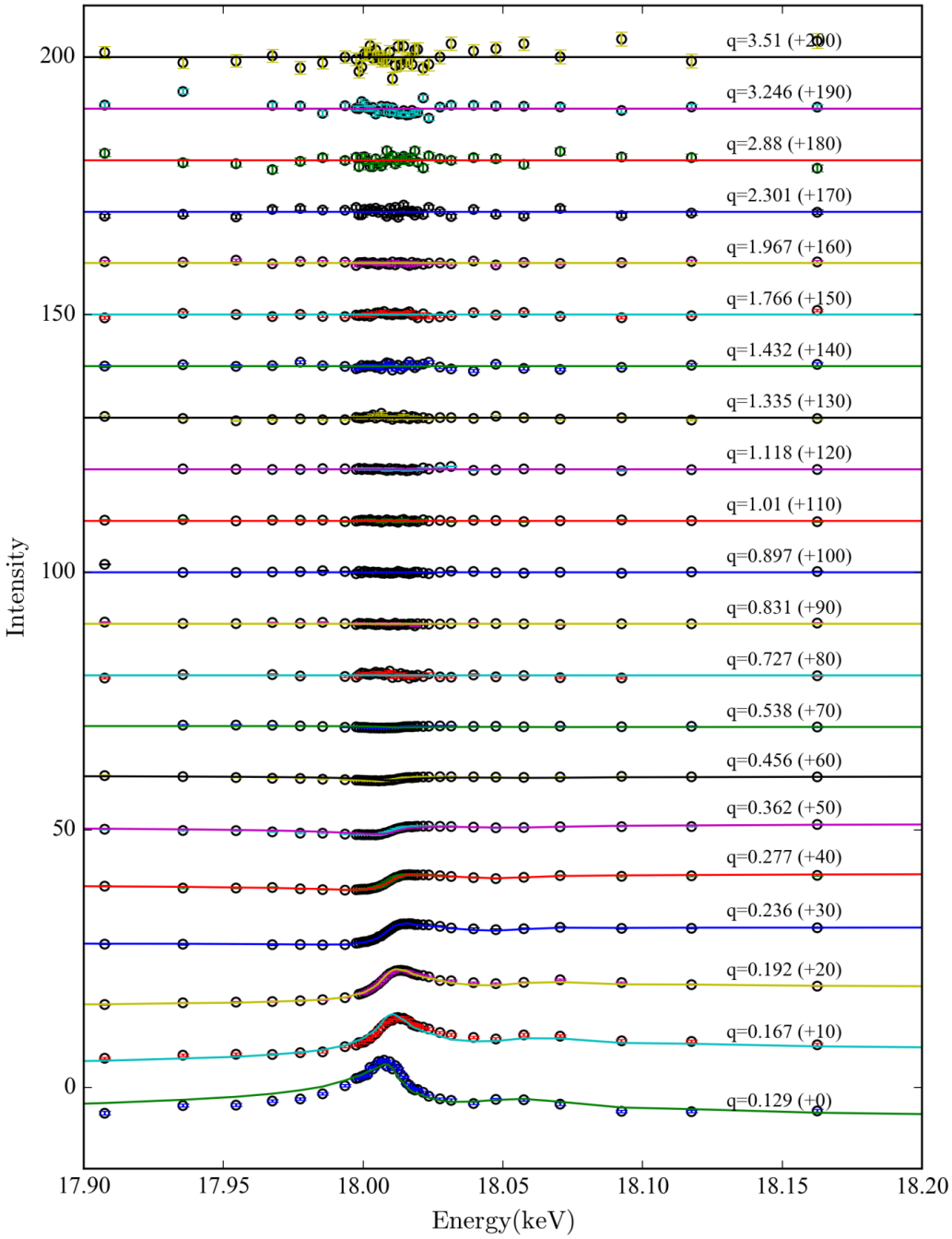

Figure S3. Full set of Zr RAXR data (open dots) for the sample containing 0.1 M LiCl measured for Zr(IV) adsorption on mica (001) surface as well as the calculated RAXR profiles (model dependent results) from the best fit model (solid lines). Each spectrum presents the variation of specular reflectivity as a function of photon energy, E, at different momentum transfer *q*. The specular reflectivity (data point and calculated values) at each *q* for different cases are offset accordingly to make better visibility.

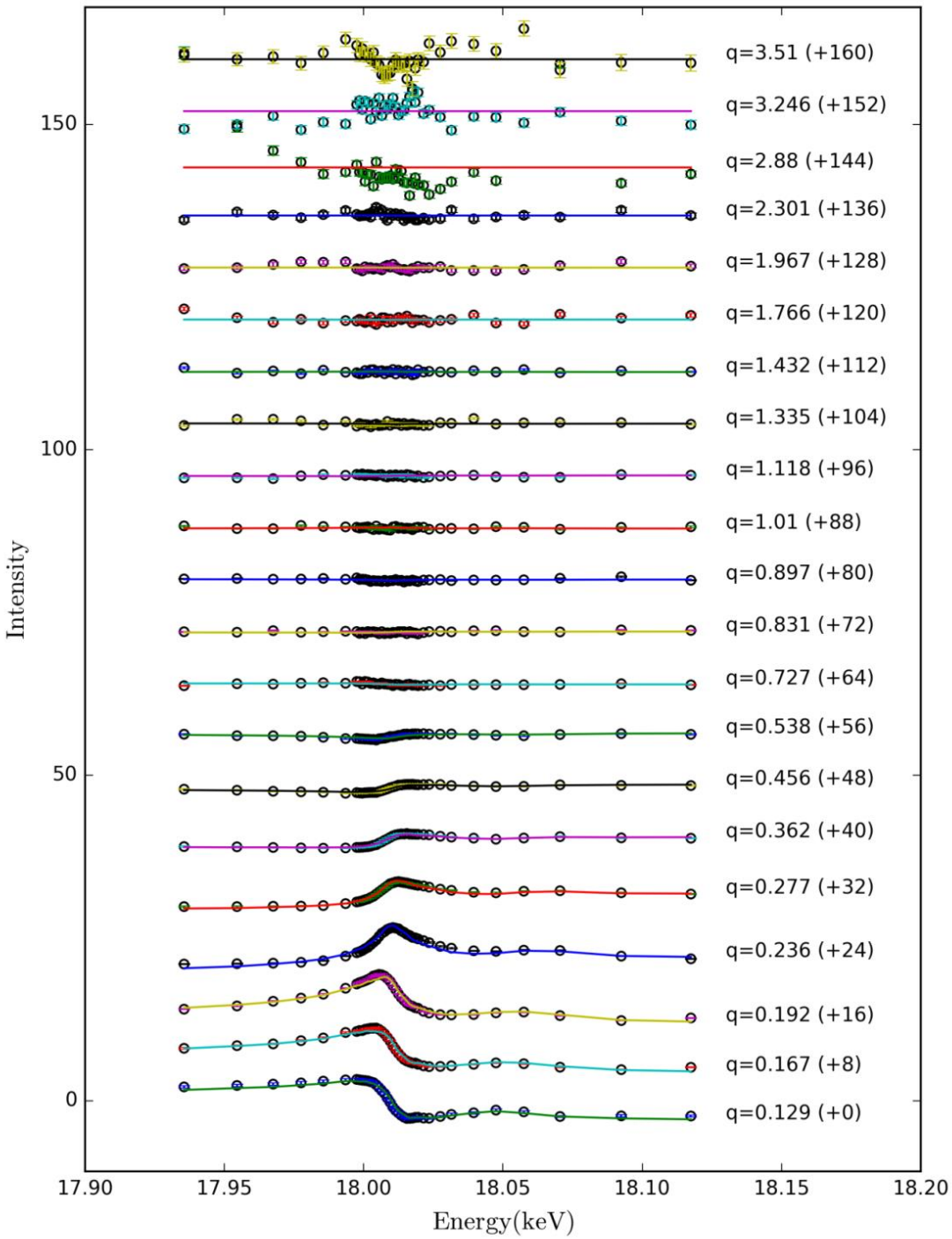

Figure S4. Full set of Zr RAXR data (open dots) for the sample containing 0.1 M NaCl measured for Zr(IV) adsorption on mica (001) surface as well as the calculated RAXR profiles (model dependent results) from the best fit model (solid lines). Each spectrum presents the variation of specular reflectivity as a function of photon energy, E, at different momentum transfer *q*. The specular reflectivity (data point and calculated values) at each *q* for different cases are offset accordingly to make better visibility.

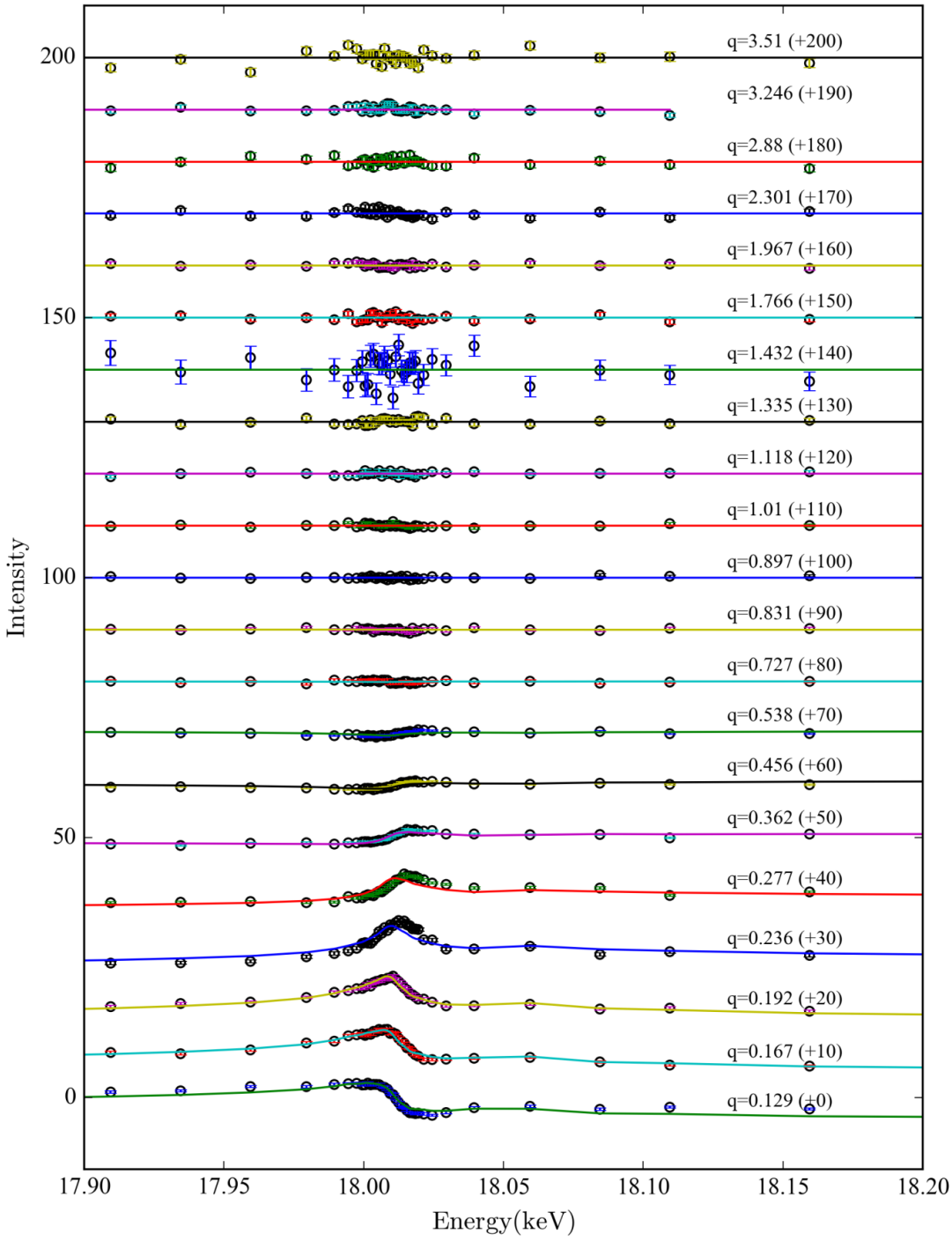

Figure S5. Full set of Zr RAXR data (open dots) for the sample containing 0.1 M KCl measured for Zr(IV) adsorption on mica (001) surface as well as the calculated RAXR profiles (model dependent results) from the best fit model (solid lines). Each spectrum presents the variation of specular reflectivity as a function of photon energy, E, at different momentum transfer *q*. The specular reflectivity (data point and calculated values) at each *q* for different cases are offset accordingly to make better visibility.

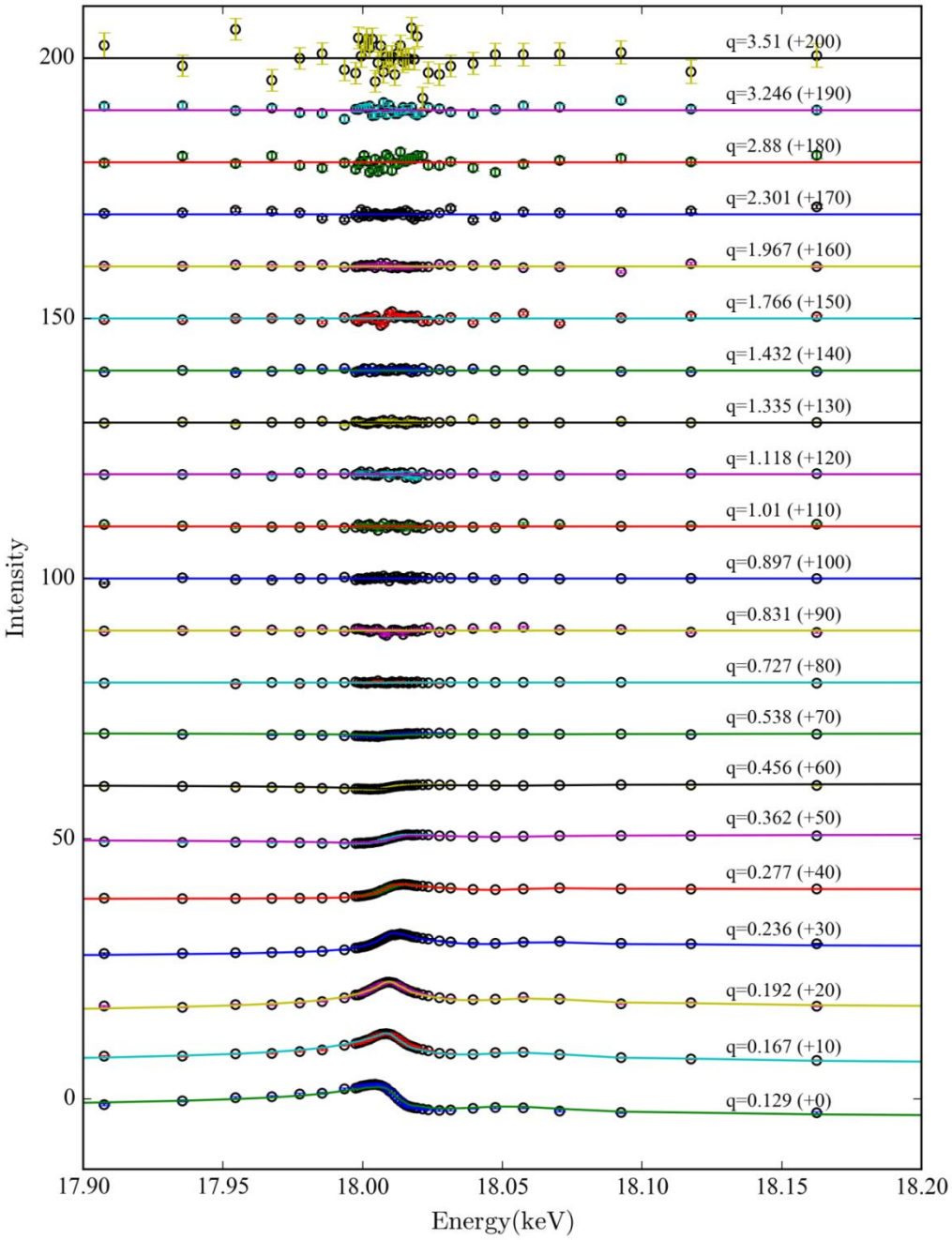

Figure S6. Full set of Zr RAXR data (open dots) for the sample containing 0.1 M RbCl measured for Zr(IV) adsorption on mica (001) surface as well as the calculated RAXR profiles (model dependent results based on one Zr peak structure model) from the best fit model (solid lines). Each spectrum presents the variation of specular reflectivity as a function of photon energy, E, at different momentum transfer *q*. The specular reflectivity (data point and calculated values) at each *q* for different cases are offset accordingly to make better visibility.

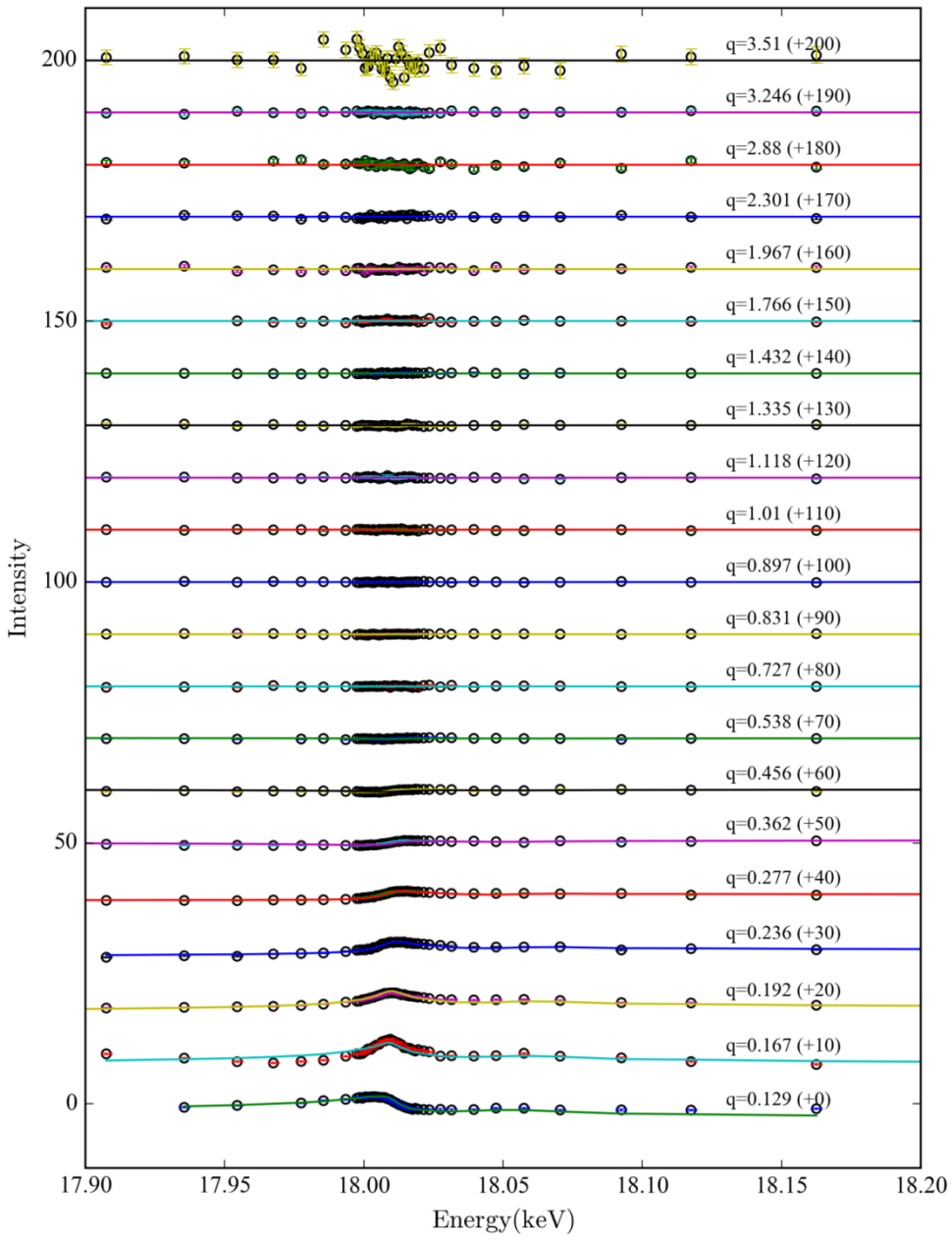

Figure S7. Full set of Zr RAXR data (open dots) for the sample containing 0.1 M CsCl measured for Zr(IV) adsorption on mica (001) surface as well as the calculated RAXR profiles from the best fit model (solid lines). Each spectrum presents the variation of specular reflectivity as a function of photon energy, E, at different momentum transfer *q*. The specular reflectivity (data point and calculated values) at each *q* for different cases are offset accordingly to make better visibility.

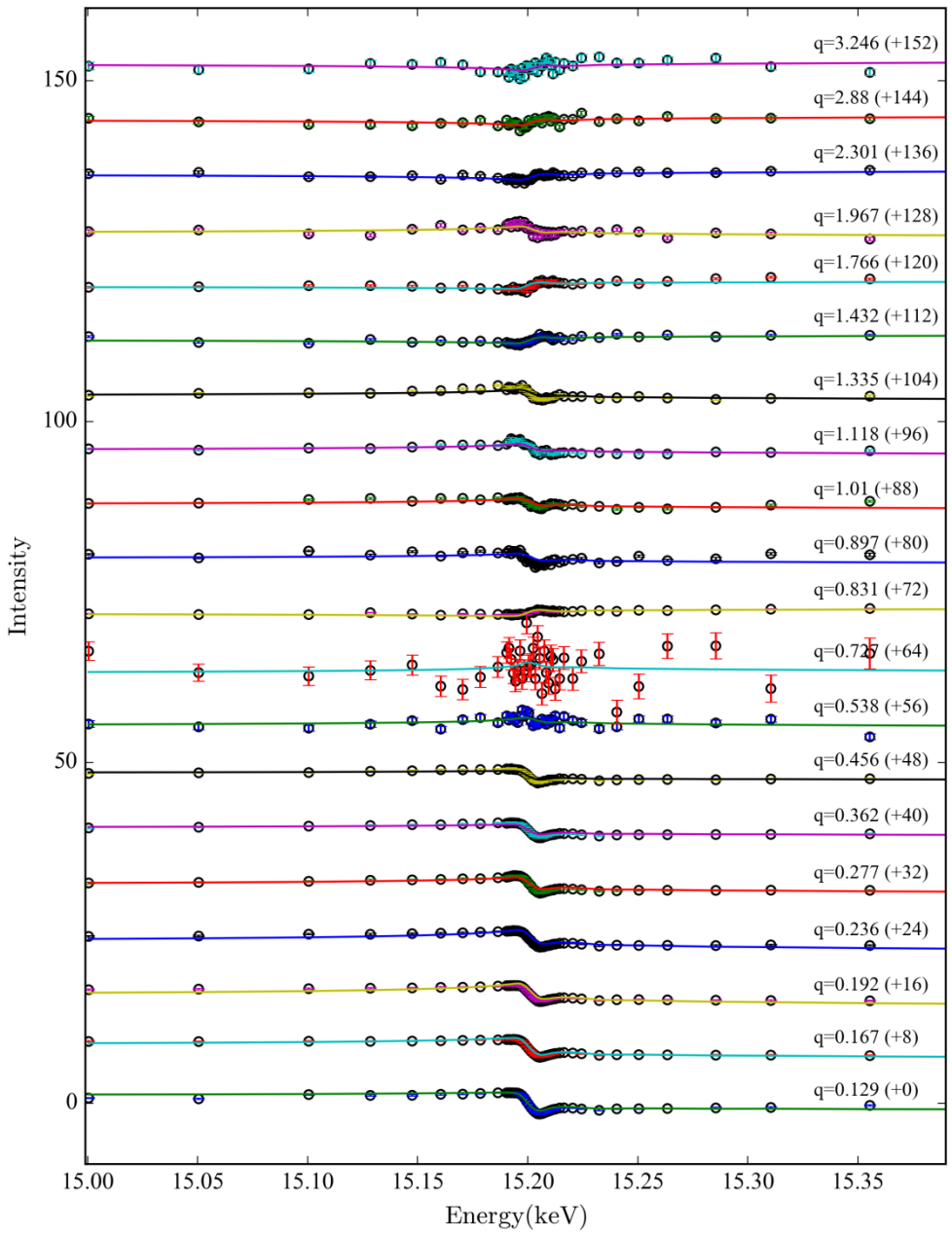

Figure S8. Full set of Rb RAXR data (open dots) for the sample containing 0.1 M RbCl measured for Zr(IV) adsorption on mica (001) surface as well as the calculated RAXR profiles Each spectrum presents the variation of specular reflectivity as a function of photon energy, E, at different momentum transfer *q*. The specular reflectivity (data point and calculated values) at each *q* for different cases are offset accordingly to make better visibility.

5. Horizontal AFM profiles

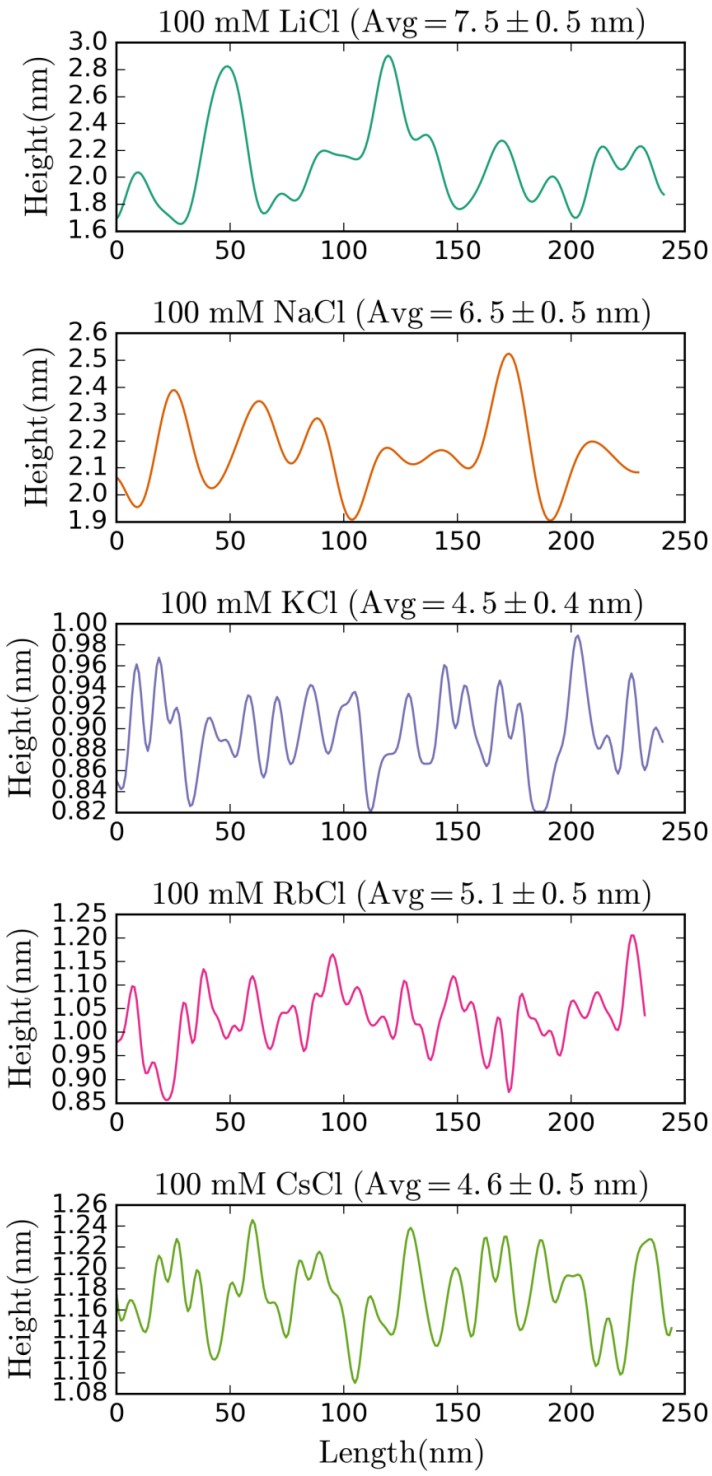

Figure S9. Lateral dimension analysis results through splitting the one-dimensional texture into waviness (the low-frequency components defining the overall shape) and roughness (the high-frequency components) at the cut-off frequency.[6] One representative waviness profile is

shown for each sample, while the average wavelength for each sample is calculated through results of 12 different profiles.

6. CTR fitting results

Table S1 Fitting parameters and uncertainties of the best fit CTR/RAXR model for Zr-mica sample at different ionic strength[1]

Model 1: Zr-mica under 100 mM LiCl (χ^2_{CTR}=13.3, χ^2_{RAXR}=3.32, R_{CTR}=13.38%, R_{RAXR}=3.8%)

		Interfacial structure			Layered water structure			
		$z_{i\ (Å)}$	$u_{i\ (Å)}$	c_i	$z_{w1(Å)}$	d	$u_{w1(Å)}$	du
CTR		13.3(0.3)	8.41(0.91)	9.389(0.766)	2.313(0.025)	3.383(0.147)	0.872(0.029)	**1.5**
RAXR	r	13.139(0.063)	4.872(0.089)	3.736(0.091)	-			

Model 2: Zr-mica under 100 mM NaCl (χ^2_{CTR}=7.3, χ^2_{RAXR}=8.58, R_{CTR}=10.05%, R_{RAXR}=3.86%)

		Interfacial structure			Layered water structure			
CTR		O	2.613(.060)	0.309(.068)	1.848(.052)	**2.454**	0.715(.082)	**0.991**
		O	9.972(.289)	3.790(.218)	-			
		O	18.587(2.603)	3.549(2.017)				
RAXR	r	Zr	10.279(.088)	4.460(.135)				
	r	Zr	22.347(.366)	1.212(.484)				

Model 3: Zr-mica under 100 mM KCl (χ^2_{CTR}=20.8, χ^2_{RAXR}=3.68, R_{CTR}=21.23%, R_{RAXR}=3.42%)

		Interfacial structure			Layered water structure			
CTR		8.62(0.17)	6.0(0.5)	7.48(0.72)	2.54(0.08)	2.954(0.464)	0.915(0.115)	**2.122**
		18.576(0.531)	0.801(0.282)	4.561(1.216)	-			
RAXR	r	10.148(0.081)	3.954(0.091)	3.071(0.083)				

Model 4: Zr-mica under 100 mM RbCl (χ^2_{CTR}=6.687, $\chi^2_{RAXR\_Zr}$=2.134, $\chi^2_{RAXR\_Rb}$=3.037, R_{CTR}=12.05%, R_{RAXR_Zr}=1.42%, R_{RAXR_Rb}=4.11%)

		Interfacial structure			Layered water structure			
CTR		2.029(0.036)	1.46(0.35)	0.307(0.204)	3.1(0.4)	**2.0**	0.947(0.195)	1.135(0.402)
		11.152(0.228)	4.96(0.46)	7.609(0.449)	-			
RAXR	r	11.246(0.054)	4.312(0.078)	2.422(0.047)				
	b	1.94(0.02)	0.2(0.1)	0.61(0.02)				
	b	14.8(0.1)	1.5(0.1)	0.42(0.03)				
	b	0.6(0.1)	5.8(0.2)	2.5(0.1)				

Model 5: Zr-mica under 100 mM CsCl (χ^2_{CTR}=19.13, χ^2_{RAXR}=2.44, R_{CTR}=15.95%, R_{RAXR}=2.68%)

	Interfacial structure			Layered water structure			
CTR	3.11(0.37)	0.706(0.235)	1.25(0.936)	2.118(0.051)	2.781(0.187)	0.442(0.042)	0.913(0.139)
	10.694(0.459)	5.059(1.222)	6.339(0.846)				
	20.754(1.003)	1.39(0.56)	6.133(1.444)	-			
RAXR	11.639(0.091)	4.793(0.133)	1.776(0.061)				

[1] z_j, c_j, and u_j: height from the muscovite surface, occupancy, and distribution width of the jth peak (j = 1−3). Occupancies (c_j) are normalized to one unit cell in a unit of number of atoms per unit cell (of which the O peaks are further normalized to the equivalence of water molecule per unit cell). z_{w1} is the height of first water layer from the mica surface, d the distance between two adjacent water layer, u_{w1} the distribution width of 1st water layer peak, du is the stepwise increase of distribution width of layer water extending towards featureless bulk water region. Numbers inside parentheses are the statistical errors for the best fit parameter values obtained from the non-square least refinement process. Underscored numbers are fixed during fitting process.

References

1. Schmidt, M.; Eng, P.; Stubbs, J.; Soderholm, L.; Fenter, P., On a new X-ray reflectivity environmental cell design for in situ studies of radioactive and atmosphere-sensitive samples. *Rev. Sci. Instrum.* **2011,** *82* (7), 075105-1 - 075105-10.
2. Schlegel, M. L.; Nagy, K. L.; Fenter, P.; Cheng, L.; Sturchio, N. C.; Jacobsen, S. D., Cation sorption on the muscovite (0 0 1) surface in chloride solutions using high-resolution X-ray reflectivity. *Geochim. Cosmochim. Ac.* **2006,** *70* (14), 3549-3565.
3. Fenter, P., X-ray Reflectivity as a Probe of Mineral-Fluid Interfaces: A User Guide. *Rev. Mineral. Geochem.* **2002,** *49*, 149-220.
4. Lee, S. S.; Nagy, K. L.; Fenter, P., Distribution of barium and fulvic acid at the mica–solution interface using in-situ X-ray reflectivity. *Geochim. Cosmochim. Ac.* **2007,** *71*, 5763-5781.
5. Cheng, L.; Fenter, P.; Nagy, K. L.; Schlegel, M. L.; Sturchio, N. C., Molecular-Scale Density Oscillations in Water Adjacent to a Mica Surface. *Phys. Rev. Lett.* **2001,** *87* (15), 156103.
6. Nečas, D.; Klapetek, P., Gwyddion: an open-source software for SPM data analysis. *Open Phys.* **2012,** *10* (1), 181-188.
7. Richter, C., Müller, K., Drobot, B., Steudtner, R., Großmann, K., Stockmann, M. and Brendler, V., Macroscopic and spectroscopic characterization of uranium (VI) sorption onto orthoclase and muscovite and the influence of competing Ca2+. *Geochimica et Cosmochimica Acta*. **2016**, 189, 143-157.
8. Arnold, T.; Utsunomiya, S.; Geipel, G.; Ewing, R. C.; Baumann, N.; Brendler, V., Adsorbed U(Vi) Surface Species on Muscovite Identified by Laser Fluorescence Spectroscopy and Transmission Electron Microscopy. *Environmental Science & Technology* **2006**, *40*, 4646-4652.

9. Schlegel, M. L.; Nagy, K. L.; Fenter, P.; Cheng, L.; Sturchio, N. C.; Jacobsen, S. D., Cation Sorption on the Muscovite (0 0 1) Surface in Chloride Solutions Using High-Resolution X-Ray Reflectivity. *Geochimica et Cosmochimica Acta* **2006**, 70, 3549-3565.

10. Lee, S. S.; Fenter, P.; Nagy, K. L.; Sturchio, N. C., Changes in adsorption free energy and speciation during competitive adsorption between monovalent cations at the muscovite (001)-water interface. *Geochimica et Cosmochimica Acta* **2013,** *123*, 416-426.